6-2007

Influence of lithophysal geometry on the uniaxial compression of tuff-like rock

Douglas B. Rigby
University of Nevada, Las Vegas

Moses Karakouzian

Amy J. Smiecinski
University of Nevada, Las Vegas, smiecins@unlv.nevada.edu

Nevada System of Higher Education

TECHNICAL REPORT

Influence of Lithophysal Geometry on the Uniaxial Compression of Tuff-Like Rock

Report Document Identifier:

TR-07-001

Task ORD-FY04-013

REVISION: 0

Author:	Douglas B. Rigby	[redacted] (signature)	06/13/07 date
PI:	Moses Karakouzian	[redacted] (approval signature)	06/13/07 date
QA Manager:	Amy J. Smiecinski	[redacted] (approval signature)	6-13-07 date

1.0 TABLE OF CONTENTS

LIST of FIGURES

LIST OF TABLES

2.0 PURPOSE

2.1 Purpose. The purpose of this report is to summarize the work and present conclusions of Project Activity Task **ORD-FY04-013** conducted under Cooperative Agreement No. DE-FC28-04RW12232 between the U.S. Department of Energy and the Nevada System of Higher Education (NSHE). This document describes results of laboratory testing on analog lithophysal tuff (Hydro-StoneTB®) conducted in the Department of Civil and Environmental Engineering of the University of Nevada at Las Vegas (UNLV) from 2004 to 2006.

2.2 Scope. The scope of this report includes documentation of the study's purpose, methods, results, conclusions, recommendations, and intended use of the data. In particular, the report will provide:

- a description of the analog rock material chosen as most similar to Topopah Spring lithophysal tuff at Yucca Mountain (Section 7.1),
- a description of the systematic experimental study planned as part of this task to quantify and study the affects of lithophysal (void) geometry on the uniaxial mechanical properties of the analog rock. (Section 7.2),
- a summary of the uniaxial mechanical properties found for the lithophysal analog rock (uniaxial compressive strength and Young's modulus), including their uncertainties (Section 7.2), and
- conclusions as to whether the analog rock data helps to validate Yucca Mountain numerical models and assumptions (Section 7.3),

2.3 Limitations. The inputs, assumptions, determinations of geotechnical parameters, and references presented in this report are deemed to be complete and accurate. However, the correct use of these results in the context of the Yucca Mountain project depends on the validity of two assumptions discussed further in Section 6:

1. The basic conceptual model of lithophysal rock consists of solid rock and open macroscopic holes and that the lithophysal (or void) porosity is the most significant variable affecting the mechanical properties of lithophysal rock.
2. Analog lithophysal rock behaves mechanically in all key aspects (e.g., deformation, crack initiation and propagation, nature of failure) like Yucca Mountain lithophysal tuff.

It should also be noted that these results reflect uniaxial compressive loading only. No tensile or confined specimen tests were conducted as part of this research.

3.0 QUALITY ASSURANCE

3.1 This work was conducted in accordance with the NSHE Quality Assurance Program. No subtask status was changed to non-Q. All conclusions of this report were based on qualified data (013DR.002) and no conclusions were based solely on unqualified data.

4.0 INTRODUCTION

4.1 Abstract

A large portion of the rock of the high-level nuclear waste repository at Yucca Mountain contains lithophysae or voids. These voids have a significant detrimental effect on the engineering properties of the rock mass and its performance. The lithophysae were formed at the time of volcanic deposition by pockets of gas trapped within the compressing and cooling pyroclastic flow material. Lithophysae vary by size, shape, and spatial frequency of occurrence. Due to the difficulties of testing actual lithophysal rock, the current mechanical property data set is limited and the numerical models of lithophysal rock are not well validated.

The purpose of this task was to experimentally quantify the effect of void geometry in the mechanical compression of cubes of analog lithophysal-like rock. In this research the mechanical properties of the analog rock were systematically studied by examining various patterns of voids based on variables consisting of hole shape, size, and geometrical distribution. Each specified hole pattern was cast into 6 by 6 by 6-in. Hydro-StoneTB® specimens (produced in triplicate) and then tested under uniaxial compression. Solid Hydro-StoneTB® specimens exhibited similar mechanical properties to those estimated for rock mass solid specimens of Topopah Spring tuff.

The results indicated that the compressive strength and Young's Modulus values decrease with increasing specimen void porosity. The modulus and strength with void porosity relationships are essentially linear over the 5 to 20 percent void porosity range. When zero void porosity (solid specimen) results are added, exponential functions do not provide a good fit to the data due to a significant sensitivity of strength and modulus to the presence of macro-sized voids. From solid specimens there is roughly a 60 percent drop in strength with about 7 percent void porosity, increasing to an 80 percent drop at about 20 percent void porosity. The percent change in modulus from the solid specimen value is roughly 30 and 45 percent at 7 and 19 percent void porosity, respectively. A bilinear model gives a much better fit to the observed experimental data.

Shape of hole appears to be significant for strength, but not for Young's Modulus. Size of hole (at similar values of porosity) does not effect modulus values, but there may be a correlation with strength (smaller hole specimens are slightly stronger). Overall, the results help to validate the Yucca Mountain numerical model of lithophysal rock, but there are also some differences that should be looked into and explained. Hydro-Stone TB® specimens give mechanical strength results that are about one rock mass category lower than is expected based on their lithophysal porosity.

4.2 Background

Experience constructing tunnels in lithophysal rock and the numerical modeling of the mechanical behavior of this rock is limited. Nevertheless, current plans call for approximately 85 percent of the proposed repository emplacement area at Yucca Mountain to be constructed within lithophysal rock (Rigby, D.B., et. al. 2003, Section 5.4, p. 5-20). Lithophysae are (gas) cavities in volcanic tuff, which weaken the rock considerably. The lithophysal rocks contain up to 30% or higher lithophysal (or void) porosity, but typically less than 20%. Lithophysal porosity is defined as the fractional volume of large-scale (centimeters-meters) void space per unit volume of rock. Visual

inspection of lithophysal rock penetrated by exploratory tunnels at Yucca Mountain indicates rock that appears sufficiently competent for safe storage of high-level waste. Some of the lithophysal rock is largely fracture free (Tptpul) while other areas typically have a ubiquitous fracture pattern (Tptpll). This research focuses on analog lithophysal rock that is initially fracture free.

Lithophysal rock-mass properties are size-dependent due to the presence of voids. The extensive project testing of small cores of lithophysal rock are not representative of rock-mass properties, as the small specimen diameter (generally 51 mm or 2 in) precludes a reasonable sampling of the lithophysal voids. As such, smaller specimens reflect higher strength and stiffness properties than is expected for lithophysal rock mass.

To study this issue, the project tested a number of larger specimens of lithophysal rock, cores of 267 and 290 mm (10.5 and 11.5 in.) diameter, in uniaxial compression, in order to discover the strength and deformation characteristics of lithophysal rock. Some 6 by 6 by 6-in. cubical specimens of lithophysal tuff have also been tested. These tests show that the mechanical properties are primarily a function of lithophysal porosity, although the specimen values of lithophysal porosity are not known with much certainty and the geometry of voids are not known. There remains a distinct lack of test data at a scale that is relevant for the full characterization of lithophysal rock.

The effect of void geometry (shape, size, and distribution) on mechanical properties has been modeled numerically, but these results have not been validated by experimental testing. Numerical models of lithophysal rock were developed using two discontinuum computer programs, PFC2D (Particle Flow Code) and UDEC. Compression tests of numerical lithophysal rock models, some having dimensions as large as 1 m by 1 m, were conducted. Of special relevance to this research, a plane strain numerical "shape study" was carried out using simulated rock with void patterns based on different uniform shapes and actual geometry to predict the influence of void geometry on mechanical properties (Figures 4-1 and 4-2 shows predictions for circles, spheres, and stenciled actual lithophysae). This work is documented in Section 6.5 of *Lithophysal Rock Mass Mechanical Properties of the Repository Host Horizon* (Rigby, D.B. 2004). It was concluded that the shape, size, and geometrical pattern of voids are significant for mechanical properties. It was postulated that ultimate strengths, in particular, appear to depend importantly on the average "bridge length" present in the numerical rock specimen. Fractures were seen to form in the numerical models of rock between voids having the shortest bridge length, which represents the shortest dimension of solid rock between voids (or from void to an edge of the specimen). There was also a tendency for vertical axial splitting between holes (and from specimen edges) and shear along diagonal sections of the specimen. Failure in numerical specimens typically consists of a progression of fractures propagating in some pattern within the specimen until ultimate failure is reached.

The above numerical models of lithophysal rock are relied upon for confidence in bounding the mechanical rock mass properties of specific lithophysal rock units at Yucca Mountain (Rigby, D.B. 2004, *Lithophysal Rock Mass Mechanical Properties of the Repository Host Horizon*, Section 6.6). This is seen in Figure 4-1 where the dark red lines indicate the bounding ranges of uniaxial compressive strength (UCS) and Young's Modulus with void porosity. Notice that both lithophysal rock tests and numerical tests appear in the figure to help justify the bounds. The numerical model also forms the basis for predicting the degradation and rock fall in repository storage drift tunnels thousands of years into the future (Kicker, D. 2004, *Drift Degradation Analysis)*.

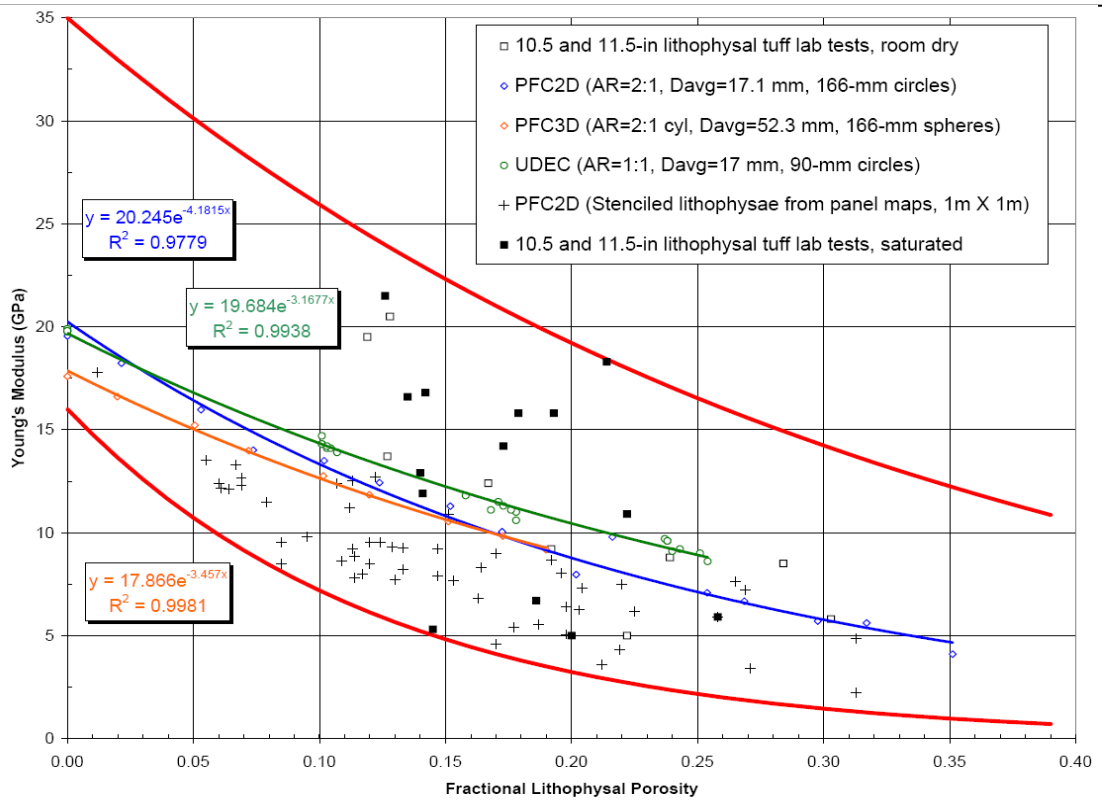

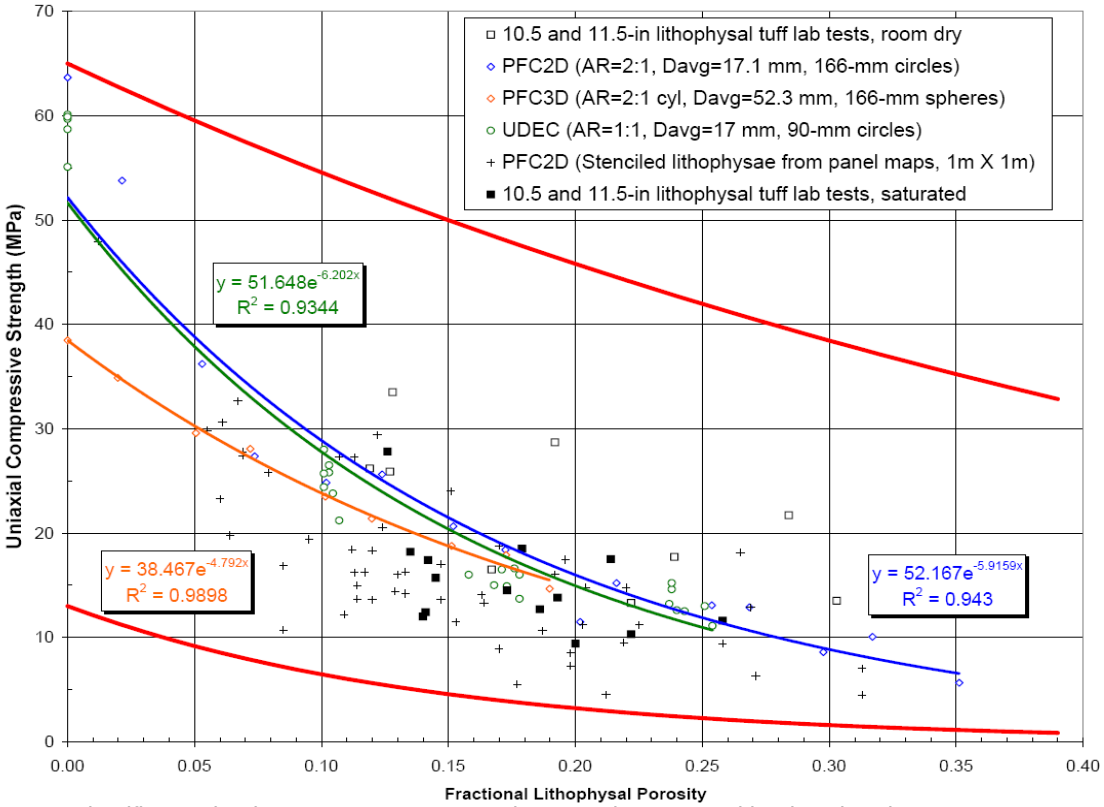

Source: Scientific Notebook UCCSN-UNLV-073 Vol. 2, Attachment H, "LithophysalRockRanges_UNLV_Task13.xls", worksheets "E-por" (top) and "q-por" (bottom). For information only; not to be used for quality-affecting work.

Figure 4-1. Young's Modulus versus Lithophysal Porosity Relationship (top) and Uniaxial Compressive Strength versus Lithophysal Porosity (bottom) for Large-Core Rock and Numerical Model Results (UQ)

When data in Figure 4-1 is plotted in terms of compressive strength vs. Young's modulus the relationships in Figure 4-2 are obtained. Note that the large-core lithophysal rock testing yields a roughly linear result, while the numerical modeling predicts an exponential relationship. One unresolved issue is which relationship is the correct one for lithophysal rock? Might there be a problem with the numerical models?

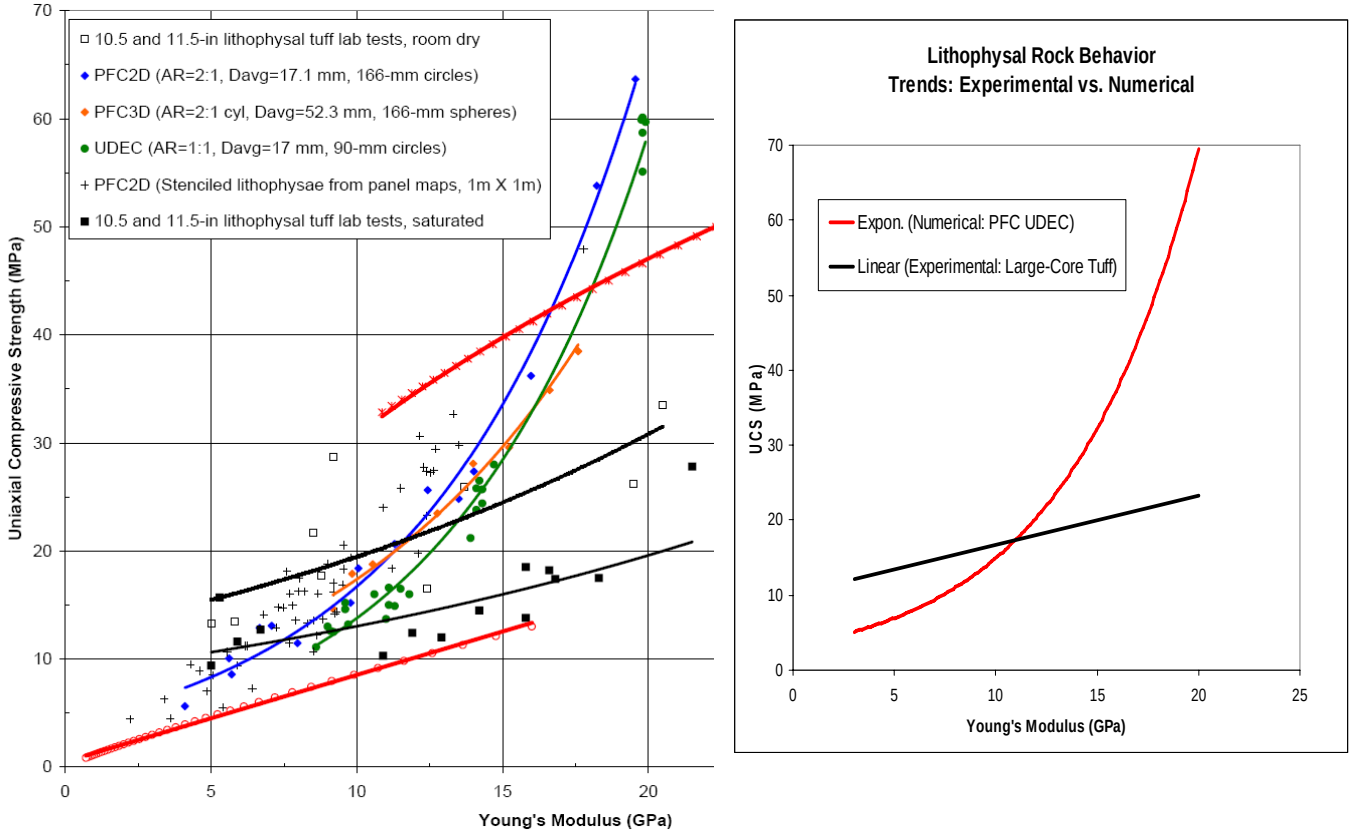

Source: Scientific Notebook UCCSN-UNLV-073 Vol. 2, Attachment H, "LithophysalRockRanges_UNLV_Task13.xls", worksheet "q-E". Figure to right is just a composite rough sketch of the two trends. For information only; not to be used for quality-affecting work.

Figure 4-2. Young's Modulus versus Uniaxial Compressive Strength for Large-Core Rock and Numerical Model Results (UQ)

Because YM project personnel believed it was important to validate aspects of the numerical model of lithophysal rock, this co-op project with UNLV was funded in order to systematically and quantitatively determine the compressive strength and Young's Modulus values of lithophysal-like rock with known shape, size, and geometry of voids. This new experimental data could then be used to validate the "shape study" and other numerical predictions from the numerical model.

The summary of data resulting from this task is stored in the NSHE Technical Data Archive under NSHE Data ID No. 013DR.002. All QA data and conclusions presented in this report are based on the 013DR.002 data set. Other supporting details and information, such as photos, nature of cracking, etc., can be found in the scientific notebook (and electronic files) UCCSN-UNLV-073 Vol. 2 associated with this project.

4.3 Brief Literature Review

R. Price of Sandia National Laboratories, issued reports in 1983, 1986 and 2004 that discussed the mechanical properties of lithophysal tuff as part of older and more recent experiments. All of the studies indicated that porosity is the primary physical property of the tuffs that can be used as a predictor of their mechanical properties. In a qualitative sense, strength and elastic modulus decreases with higher specimen porosity. However, the inherent scatter in the elastic and especially the strength properties for the welded lithophysal tuffs are large, making it difficult to establish any quantitative trends. Sample size was found to be independent of Young's modulus, but a clear trend of decreasing strength with increasing sample size was evident.

M. Karakouzian, as principal investigator, carried out research on actual specimens of lithophysal rock and studied the relationship of porosity dependence on mechanical properties of Plaster of Paris specimens with Styrofoam® inclusions as part of the Task 27 Cooperative Agreement (DE-FC28-98NV12081) between the U.S. Dept. of Energy and the University of Nevada Las Vegas (UNLV) (Avar 2003; Avar, et. al. 2003; and Hudyma, et. al. 2004). Results from both numerical models and experimental testing showed an exponential decrease in Plaster of Paris specimen strength and elastic modulus with increasing porosity, but the tuff specimens showed a linear decrease in elastic modulus and an exponential decrease in strength. Normalized strength and Young's modulus plots with porosity indicated that Plaster of Paris and tuff specimens, in general, plot along the same trend line.

Read and Hegemier (1984) surveyed rock and concrete testing research and concluded that plain concrete, like rocks, experiences the beginning of extensive macro-crack development at or slightly beyond the peak of stress-strain curve. They also found that progressive structural breakdown of the specimens began at about 50 percent of the ultimate strength. The inhomogeneous and anisotropic nature of the material on the microlevel induces local tensile stresses which produce microcracks that grow and become aligned with the loading axis. As the loading increases to 80 to 90 percent of the ultimate, the density of microcracks rapidly proliferates, leading to vertically aligned macrocracks. Beyond the peak of the stress-strain curve, the specimens were in the process of splitting and therefore could not be treated as homogeneous continua.

Hoek and Brown (1980) reviewed the literature for the influence of the diameter of a specimen (mostly igneous rocks) on the measured compressive strength. They found that sample strength increases progressively and exponentially as the sample diameter decreases.

D.J. Elwell and G. Fu (1995) surveyed the literature to compare the concrete compressive strength of cylinder and cube specimens. Cube specimens (100 or 150 mm, 4 or 6 in.) are used throughout much of Europe, including Great Britain and Germany. They found that tests on cubes and cylinders with h:d = 1 yield similar results, and so concluded that the cross-sectional shape is not significant. Past research indicates that the cylinder (2:1 h:d) to cube strength ratio to be between about 0.65 and 0.90. For higher strength concrete a higher cylinder to cube ratio is reported; one author lists a 0.85 ratio for 8000 psi (55 MPa) cube strength concrete (which is approximately the strength of solid Hydro-Stone TB® specimens).

ASTM D 4543 (2001) *Standard Practices for Preparing Rock Core Specimens and Determining Dimensional and Shape Tolerances*, and the International Society of Rock Mechanics (ISRM) procedure (1978) *Suggested Methods for Determining Uniaxial Compressive Strength and Deformability of Rock Materials* (found in Brown, 1981) recommend that the diameter of the core should be at least six to ten times that of the largest fragment/grain within the rock. By analogy, the holes in cube specimens should be six to ten times smaller than the cube dimension. For this research, the largest holes are about five times smaller than the cube length and seven times smaller than the cube diameter.

5.0 METHODS AND MATERIALS

5.1 Experimental Test Plan

Cubical shape specimens were chosen to make specimen production easier and to allow for comparing the experimental results with numerical modeled two-dimensional plane strain results. Since the holes extend all the way through the cubical specimens, the results will lie somewhere between plane strain (infinite length holes) and plane stress (thin plate) assumptions.

The following rationale was adopted for creating test specimens of analog lithophysal rock. First of all, a series of solid specimens (no holes) would be created and tested before and after all specimens with voids were created and tested. Three basic void patterns (A, B, C) were adopted, based on the location of the first hole (see Figure 5-1). Subsequent placement of additional holes was chosen randomly until the target void porosity was reached, subject to a restriction that the holes did not overlap. As a result, a sequence of holes (1, 2, 3, …), each with precise locations, was created for each pattern type (A, B, and C).

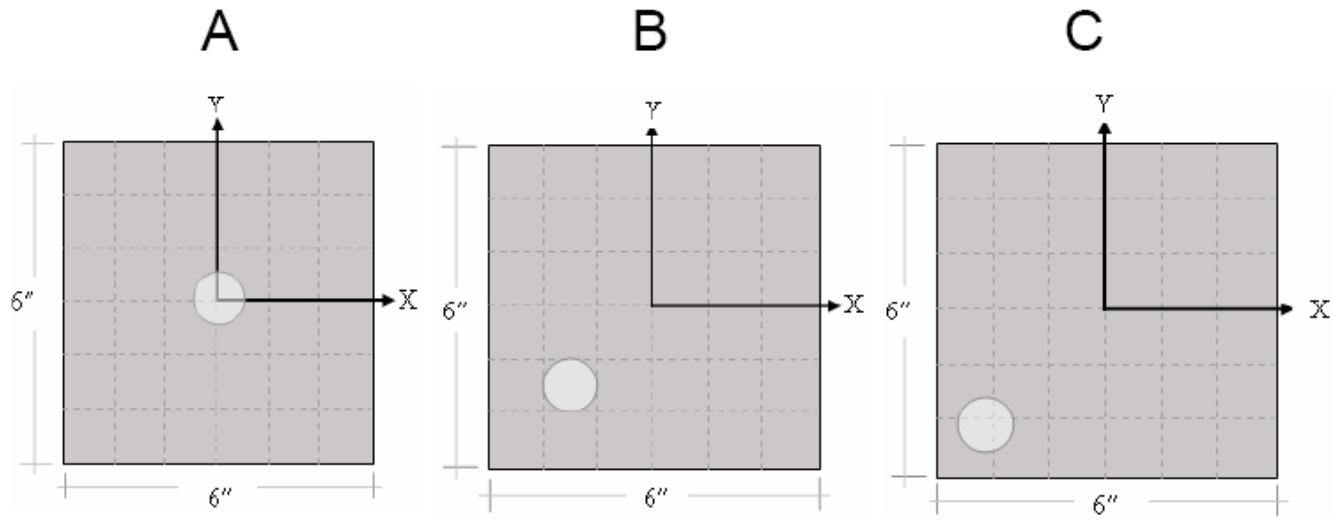

Note: First hole for pattern A is located at coordinate (0,0) in. Pattern B at (-1.5, -1.5) in. Pattern C at (-2.125, -2.125) in.

Figure 5-1. Location of First Hole for Patterns A, B, and C

For circular-hole specimens, 12 different pattern variations were planned to be implemented for each A, B, and C pattern type (see Table 5-1). These 12 pattern variations included three different size holes (nominal diameters of 1.25 in., 0.875 in., and 0.5 in) and three target porosities (nominal porosities of 7, 13 and 19 percent). Sub-patterns 1 through 3 consisted of only a uniform set of large holes, 4 through 6 only medium sized holes, and 7 through 9 only small holes. Sub-patterns 10 through 12 consisted of mixed-size holes. This gave a total of 12 specimen patterns for each A, B, or C type pattern for a total of 36 patterns. Since each pattern was produced in triplicate, a total of 108 specimens were planned with circular holes.

Similarly for square- or diamond-hole specimens, 4 different pattern variations were planned using the A and B pattern type (Table 5-2). These 4 pattern variations included two sizes of square and diamond- shaped holes and two target porosities (7 and 13 percent). The nominal side lengths of the square holes were 0.9 and 0.6 in., respectively, calculated as 0.707 times the two larger circular hole sizes. Square holes rotated 45 degrees become diamond-shape holes. The noncircular shapes allow comparison of circular versus noncircular uniaxial test results. Sub-patterns 1 and 2 consisted of large holes, and 3 and 4 medium size holes. This yielded a total of 4 square and 4 diamond specimen patterns for each A and B type pattern, for a total of 16 patterns. Since each pattern was produced in triplicate, a total of 48 specimens with square and diamond-shaped holes were planned.

The full pattern details and specimen naming convention is given in Appendix B. As can be seen in Figure B-1, the numbered hole sequence for each pattern type (A, B, or C) is always followed for determining hole positions. Holes continue to be added in a pattern until the target void porosity is reached. In other words, for pattern A, the centroid position of hole number 1 and 2 is the same for large, medium and small hole circular specimens, and for square and diamond hole specimens as well. Similarly, the centroid location of hole numbers 1, 2, 3, and so on also remain fixed for pattern B or C specimens.

Finally, a total of 166 QA specimens were created and tested according to the above plan and as part of this research: 108 circular-hole specimens, 24 square-hole specimens, 24 diamond-hole specimens, and 10 solid specimens.

Table 5-1: Specimens Containing Circular Holes (Pattern A)

Hole Shape	Starting Hole Location	Hole Size			Number of Holes	Porosity (%)	Pattern
Circle	at center (0,0)	Uniform		1.226" (L)	2	6.56	1
					4	13.12	2
					6	19.68	3
				0.870" (M)	4	6.61	4
					8	13.21	5
					12	19.82	6
				0.503" (S)	11	6.07	7
					22	12.14	8
					33	18.22	9
		Mixed	I	L	1	6.59	10
				M	1		
				S	3		
			II	L	2	14.83	11
				M	3		
				S	6		
			III	L	2	19.24	12
				M	5		
				S	8		

Source: Modified from table in scientific notebook UCCSN-UNLV-073 Vol. 2, pp. 23. "Porosity (%)" comes from DID 013DR.002, worksheet "QA Data Summary", column "DD".

Table 5-2: Specimens Containing Square or Diamond Holes (Pattern A)

Hole Shape	Starting Hole Location	Hole Size		Number of Holes	Porosity (%)	Pattern
Square/ Diamond	at center (0,0)	Uniform	0.868" (L)	3	6.28	1
				6	12.56	2
			0.616" (M)	6	6.32	3
				12	12.65	4

Source: Modified from table in scientific notebook UCCSN-UNLV-073 Vol. 2, p. 26. "Porosity (%)" comes from DID 013DR.002, worksheet "QA Data Summary", column "DD".

5.2 Selection of Analog Rock Material

Solid rock from the Topopah Spring formation at Yucca Mountain behaves in a hard brittle manner and for rock mass solid specimens, an average Young's Modulus of about 20 GPa and an uniaxial compressive strength of about 60 MPa was estimated and used for numerical model calibration purposes (Rigby, D.B. 2004, Section 6.5.3.2, p. 6-65). In the previous cooperative agreement (Task 27) the lithophysal properties of plaster of Paris were investigated. Solid plaster of Paris had an average Young's Modulus of about 3.1 GPa (Avar, et.al. (2003), p. 925) and an uniaxial compressive strength of about 16.7 MPa (Hudyma, et.al. (2004), p. 184).

The Hydro-StoneTB® literature lists a dry compressive strength of 10,000 psi or almost 70 MPa for the material (USG Gypsums, p. 50). As part of this research, non-Q (UQ) scoping uniaxial tests on Hydro-StoneTB® specimens were conducted. It was found that 51-mm diameter cylindrical specimens had compressive strengths of almost 70 MPa as long as the specimens were completely cured (taking several weeks). Ten solid QA cubical specimens (152 mm on a side) of Hydro-StoneTB® material were tested in uniaxial compression in this task and an average Young's Modulus of 16 GPa and a strength of 55 MPa was obtained. Based on these tests, the mechanical properties and brittle behavior of Hydro-StoneTB® are similar to those estimated for solid Yucca Mountain lithophysal rock mass, accordingly, Hydro-StoneTB® was adopted as the material for analog test rock for this research.

5.3 Experimental Procedures Used

5.3.1 Specimen Preparation

Procedure IPLV-034, "Making Analog Rock Specimens for Uniaxial Testing" was followed for making, curing, and preparing analog rock test specimens of Hydro-StoneTB® in the laboratory to be used for mechanical testing. Essentially, the steps consisted of (1) mold preparation, (2) batch mixing and pouring, (3) specimen finishing, (4) mold removal, (5) curing, and (6) measuring specimen dimensions and tolerances (both flatness and perpendicularity was checked). If any specimens did not meet the dimensional tolerances they were surfaced and measured again until the tolerance criteria were met.

Plane strain holes extending through the specimen were formed by installing finished aluminum round stock or square bar in the mold before the pour. The batch was prepared by mechanical mixing of water and Hydro-StoneTB® gypsum cement at a carefully measured mass ratio of 1:3. After pouring into the mold, the mixture was vibrated to removal air bubbles. The mold was disassembled after 12 hours and the specimen allowed to cure in an environmentally-controlled laboratory ambient air environment until curing was complete (typically several weeks).

Figure 5-2 shows the specimen molds for Patterns A, B, and C. Round or square aluminum bar stock of varying dimension is attached to the opposite side of the numbered plate (shown in the figure) with socket head cap screws to create the specified void pattern for the specimen. Figure 5-3 shows a specimen being poured, and later, with the molds partially removed.

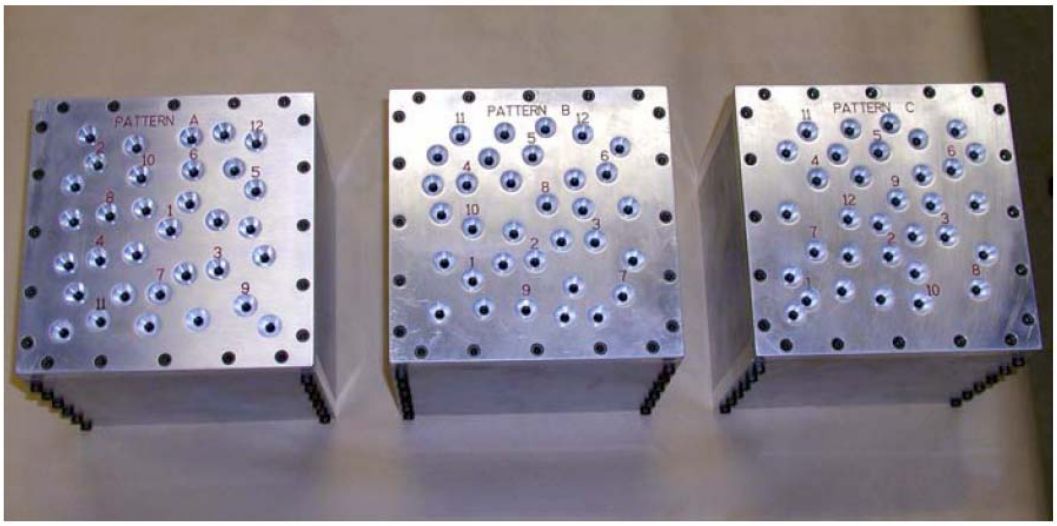

Figure 5-2. Aluminum Molds with Patterns A, B, and C Top Plates

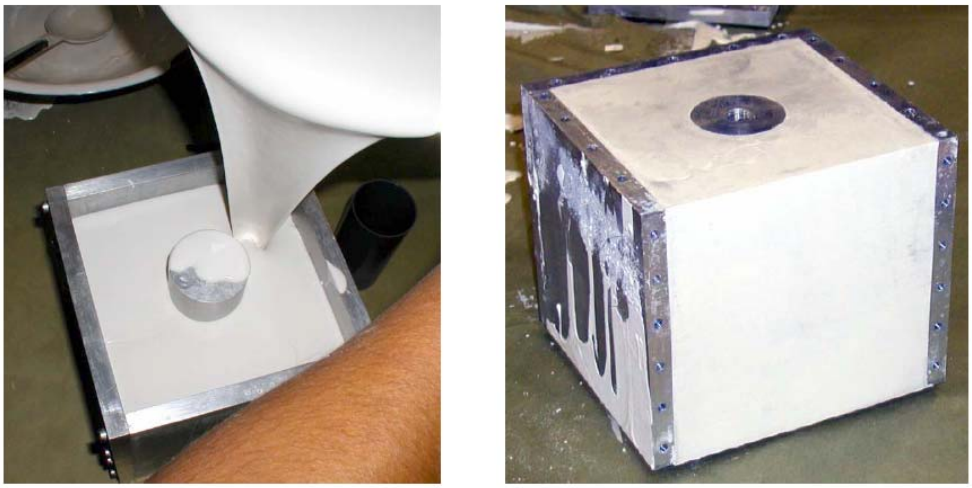

Figure 5-3. Hydro-StoneTB® Pour into Mold and Mold Partially Removed

Three specimen record sheets were used to record the details of batch mixing, curing, and dimensional measurements for each specimen. Specimens had to be fully cured and meet certain dimension tolerance criteria before they could be tested. This procedure ensured that all specimens were prepared in a uniform and consistent manner.

5.3.2 Uniaxial Compressive Testing

Procedure IPLV-057, "Test Method for Uniaxial Compressive Strength and Young's Modulus of Analog Rock Specimens," was followed to determine the uniaxial compressive strength and the elastic moduli of analog rock specimens of Hydro-StoneTB®. This procedure ensured that all specimens were tested in a uniform and consistent manner.

Testing was carried out at the Bituminous/Aggregate Labs, State of Nevada Department of Transportation, 123 E. Washington Ave., No. D., Las Vegas, Nevada. The basic testing setup included (Figure 5-4): the SATEC Series 600RD-E1 Compression Tester, a model 600K load cell, a Series 5500 Digital Controller, Basic Partner Testing Software, and two hardened (greater than 55 Rockwell hardness) steel bearing blocks. The top platen is attached to a lubricated spherical load seat and the bottom platen is a 7 in. x 7 in. x 0.5 in. flat block. The load cell was calibrated by a qualified supplier in accordance with QAP-7.0, "Control of Quality-Affecting Procurement and Receipt" and in accordance with QAP-12.0, "Control of Measuring and Test Equipment" prior to use and again following the completion of testing.

The specimen loading surfaces were not lubricated so that results would be similar to Yucca Mountain testing, which was carried out without any special lubrication. A constant loading rate of 0.012 in./min. (3.3×10^{-5} sec^{-1} strain rate) was applied until ultimate failure occurred (this represented the slowest speed achievable for this equipment). Measuring instrumentation included linear variable differential transformers (LVDTs) and a Daytronic System 10 mainframe data acquisition system. The LVDTs were calibrated prior to use, and again following the completion of testing, using procedure IPLV-051, "Calibration of Linear Variable Differential Transformers (LVDTs). The LVDTs were setup and used to measure vertical measurements in the case of specimens with voids, and both vertical and horizontal measurements of solid specimens as shown in Figure 5-4. Sketches were made to record the progressive cracking of each specimen that occurred during the test. Photographs of the specimen were taken before and after each experiment.

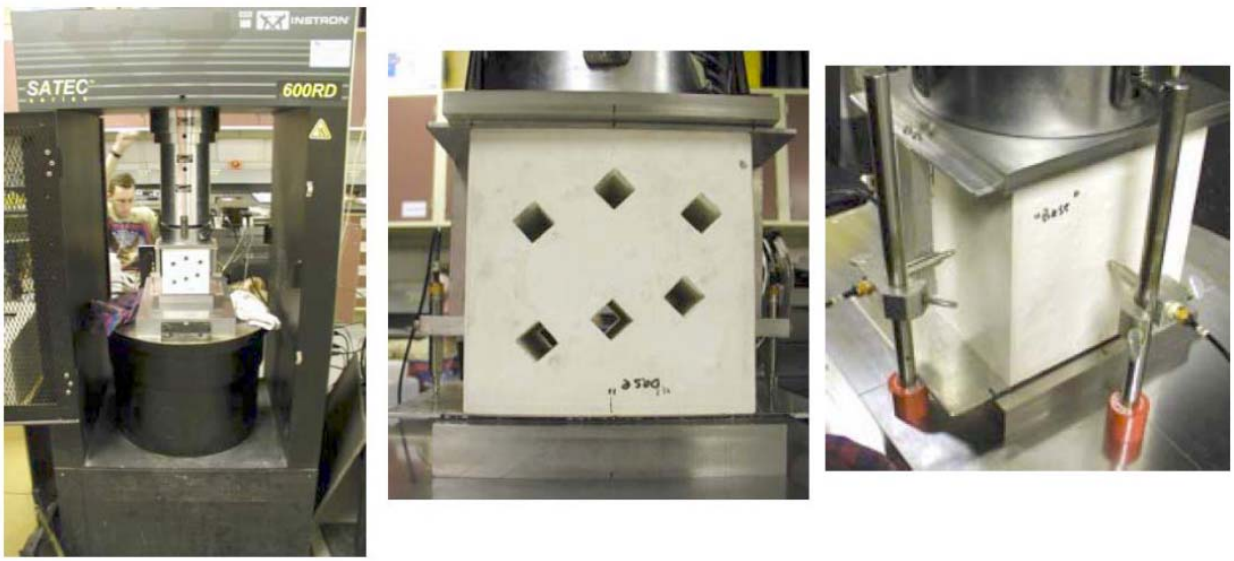

Figure 5-4. Instron Compressive Load Frame and Experimental Test Setup

5.4 Test Equipment Setup, Measurement and Experimental Uncertainty

Specimen preparation and tolerance measurements followed the procedure outlined above and made use of the following calibrated instruments with indicated measurement uncertainty: (a) OHAUS electronic scale (± 0.1 g over the range used, which was less than 13000 g), (b) ERTCO glass thermometer (± 1ºF), (c) Starrett 9-inch digital caliper (± 0.001 in.) for determining external specimen dimensions, (d) Starrett 6-inch digital caliper (± 0.001 in.) to determine hole dimensions, and (e) a CDI electronic digital indicator (± 0.0002 in.) to measure specimen flatness together with a granite flat having a surface tolerance of less than 0.0005 in. (13 μm)..

All of the specimens described in this report were tested in a large Instron 600RD load frame with a load capacity of 3000 kN (600 kips) by UNLV personnel at the Nevada Department of Transportation (NDOT) materials lab facility in Las Vegas (Figure 5-4). The machine is hydraulically driven using SATEC 5500 Series servo-control electronics with 19-bit resolution. The equipment was operated in displacement feedback control during the constant strain-rate experiments. The slowest strain rate supported by this equipment for our 6-inch specimens is about 3×10^{-5} (corresponding to about 0.012 in/min or 0.30 mm/min), controlled to within ± 0.002%. The Instron load cell force measurement accuracy is ± 0.2 % of its full-scale output. The axial and lateral displacement transducers (LVDTs) are Daytronic ± 0.1 in full-scale LVDTs and each has accuracy within ± 0.5%.

The two-dimensional void porosity was determined (the solid matrix porosity was not used) by measuring the cross-sectional dimensions of the mold rods and then calculating the porosity based on the number and size of all rods. Measurements of actual holes of cured specimens confirmed the porosity accuracies given below. The ultimate strength is the highest applied axial load measured during the experiment divided by the measured cross-sectional area of the specimen. Two LVDTs (one on each side of the specimen) measured the vertical deformation of the specimen and were averaged. Two LVDTs (one each on adjacent sides of the specimen) measured lateral deformation with respect to the center of the specimen; these measurements were doubled then averaged to obtain total deformation relative to the total specimen width. The axial and lateral strains were calculated by dividing the axial and lateral deformations by the initial specimen length and width, respectively. The Young's modulus parameters were determined as the least-square fit line of plotting the axial stress versus the axial strain data that occur between 25 and 50 percent of the ultimate specimen strength. Poisson's ratio was calculated as the least-square fit line of plotting the axial strain versus the lateral strain data that occur between 25 and 50 percent of the ultimate specimen strength.

The accuracies of the mechanical properties reported are a function of the combined accuracies of all the measuring instruments discussed above. As a result the void porosity, strength (stress), Young's moduli, and Poisson's ratio values are accurate to within ± 0.1%, ± 5%, ± 5.5%, and ± 3%, respectively.

These combined measurement and test uncertainties are small compared to scatter in the tested results due to influence of holes in the specimens. The results given in Section 7 below include statistical summaries as part of all tables of information presented. The statistical summary includes a contribution to uncertainty due to small sample sizes (3 replications).

6.0 ASSUMPTIONS

Two assumptions are important in this research. They are both germane to the issue of how analog lithophysal rock compares with natural lithophysal rock behavior under compressive loading.

6.1 Conceptual Model. The basic conceptual model of lithophysal rock consists of solid rock and air-filled macroscopic holes. The solid rock matrix is considered homogeneous and it is assumed that there are no preexisting fractures. This lithophysal (or void) porosity is assumed to be the most significant rock variable affecting the mechanical properties of lithophysal rock.

6.2 Analog Rock Behavior. The analog lithophysal rock behaves mechanically in all key respects (e.g., deformation, crack initiation and propagation, nature of failure) like Yucca Mountain lithophysal tuff. This assumption is used in Section 7.0 and the validity of the assumption will be discussed in comparisons to tested specimens in this research and those on actual lithophysal rock.

7.0 RESULTS, DISCUSSION, AND CONCLUSIONS

7.1 Discussion of Experimental Results

7.1.1 Compressive Behavior of Solid Specimens of Hydro-Stone TB®

Ten solid specimens were tested in uniaxial compression. Examples of two failed specimens are shown in Figure 7-1 and their respective stress-strain curves are plotted in Figure 7-2. Axial strain-lateral strain curves are plotted in Figure 7-3 for the same two specimens. Failure typically occurred suddenly and catastrophically. For Hydro-StoneTB® specimens, the stress-strain response was typically brittle, meaning transition from linear elastic behavior to macro-fractures and ultimate failure occurred very rapidly. Failure typically occurred at about 0.4 percent axial strain.

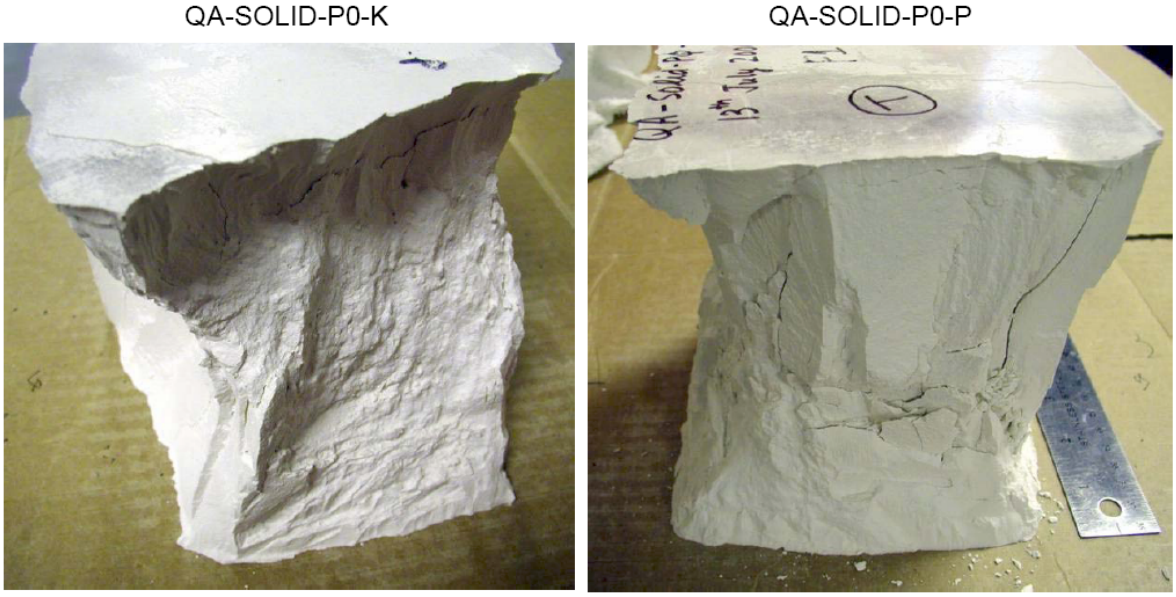

Figure 7-1. Photos of Two Solid Specimens After Testing

Each of the ten solid specimens failed suddenly, had more or less a cone failure shape as shown in Figure 7-1, and a large portion of the specimen was cracked and involved in the failure. A summary of the mechanical properties of Hydro-Stone TB® solid specimens is given in Table 7-1.

Table 7-1: Mechanical Properties of Solid Specimens

Number Specimens	Best Fit E (GPa)	E Stan. Deviation	Poisson's Ratio	ν Stan. Deviation	UCS (MPa)	UCS Stan. Deviation
10	15.98	1.07	0.28	0.05	55.01	1.61

Source: Data comes from 013DR.002; worksheet "QA Data Summary", Row 3 "QA-Solid-P0".

Note: E is best fit Young's modulus from 25 to 50% strength, Poisson's ratio is determined at 50% strength, UCS is the uniaxial compressive strength, and Stan. Deviation is the statistical standard deviation of the results.

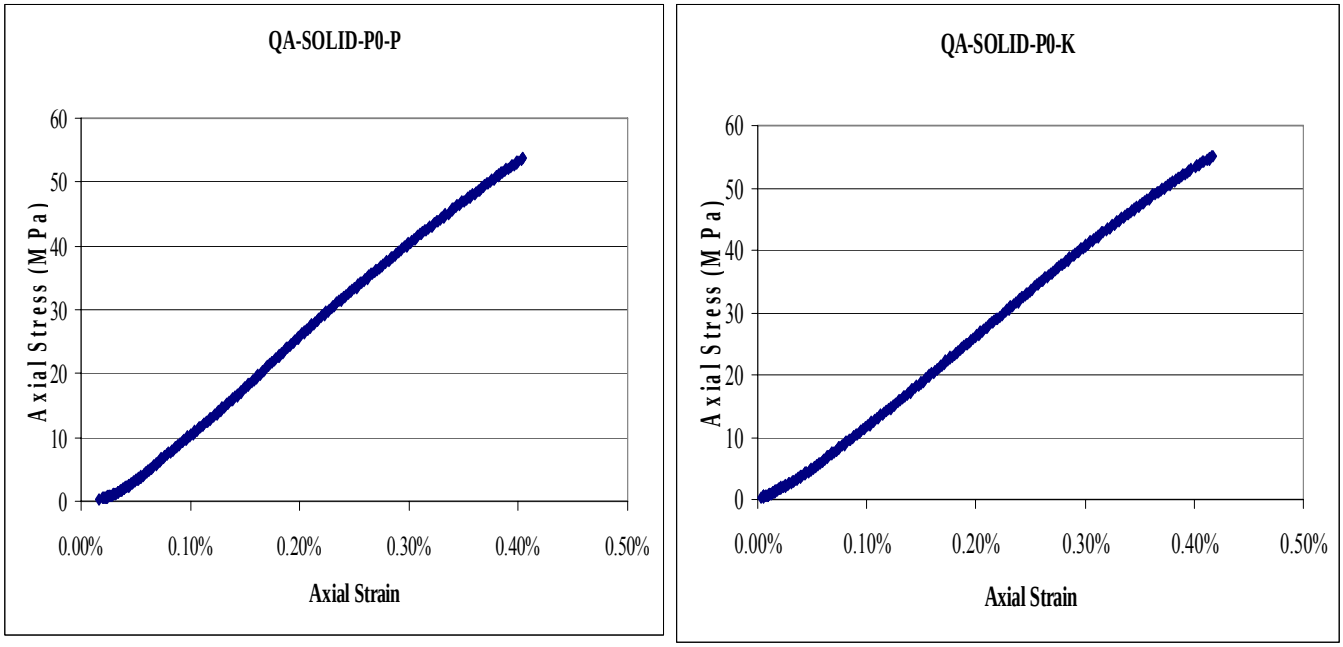

Source: Stress-strain data for tests taken from two electronic files associated with UCCSN-UNLV-073 Vol. 2: QA-SOLID-P0-P calculation.xls and QA-SOLID-P0-K calculation.xls. For information only, not to be used for quality-affecting work. Note: Strain units are in./in x 100 (percent strain).

Figure 7-2. Experimental Stress-strain Curves for Specimens QA-SOLID-P0-K and QA-SOLID-P0-P (UQ)

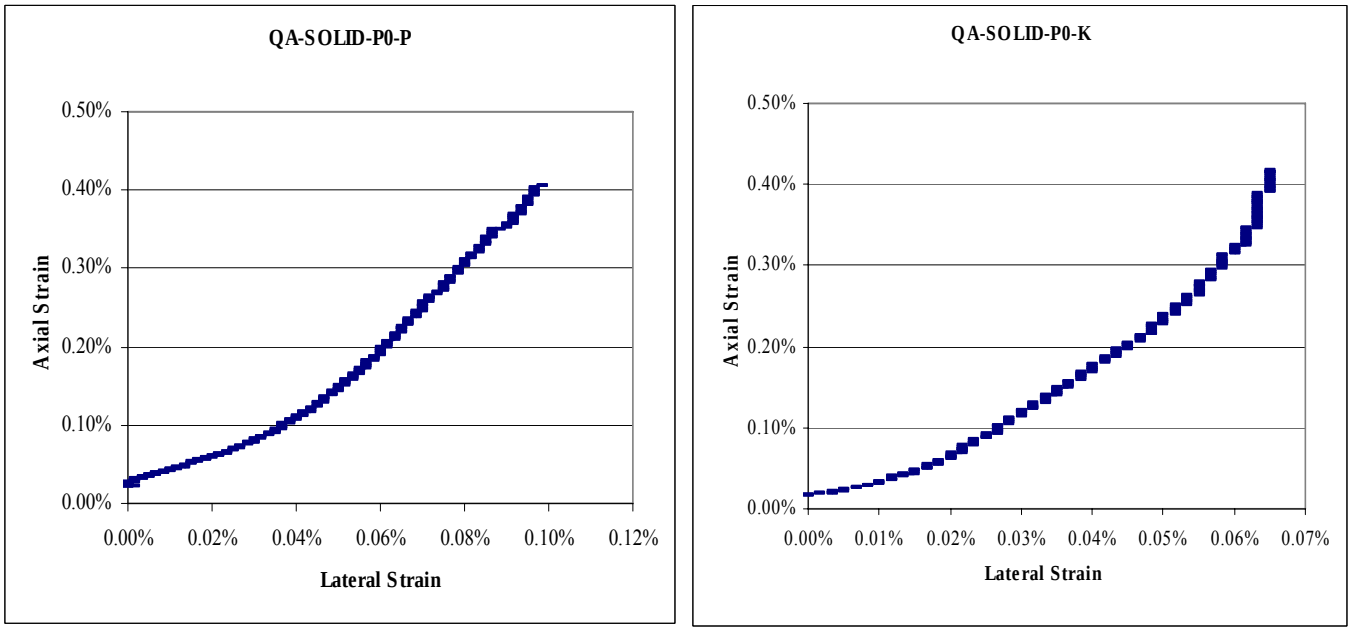

Source: Stress-strain data for tests taken from two electronic files associated with UCCSN-UNLV-073 Vol. 2: QA-SOLID-P0-P calculation.xls and QA-SOLID-P0-K calculation.xls. For information only, not to be used for quality-affecting work. Note: Strain units are in./in x 100 (percent strain).

Figure 7-3. Axial Strain-Lateral Strain Curves for Specimens QA-SOLID-P0-K and QA-SOLID-P0-P (UQ)

7.1.2 General Compressive Behavior of Specimens with Holes

General Discussion. Based on the planned patterns described in Section 5.1, 156 specimens were tested with holes. All specimens were tested at room dry and ambient temperature conditions at a constant strain rate of 3.3×10^{-5} sec^{-1}. Two examples of typical stress-strain behavior are shown in Figure 7-4, one failing suddenly (QA-PB-UCS11-P6-B) and one that failed with progressive cracking in which peak strength was achieved after a local failure had occurred (QA-PB-XCL1M1S3-P7-A). The initial non-linear portion of both curves up to about 0.05 percent strain is not due to non-linear material behavior at low stress levels but, rather, a consequence of imperfect contacts between the sample and loading platens. The stress-strain behavior is generally linear elastic up to a stress value of about 75 percent of ultimate strength.

It is likely that the first micro-fractures begin to occur during linear elastic loading. Individual test records indicate that the majority of specimens do not experience their first visible crack until a stress is reached that is more than 50% of the specimen's ultimate strength. Interestingly, for circular hole specimens, the appearance of the first crack (initiating from a hole boundary) occurred on the average at about 60% of the ultimate strength value, while for both square- and diamond-shaped holes the initial crack was noted at about 40% of ultimate strength. This is probably due to stress concentrations that occur at the relatively sharp corners of square and diamond holes, which are known to contribute to crack initiation. Of course the circular holes do not have sharp corners.

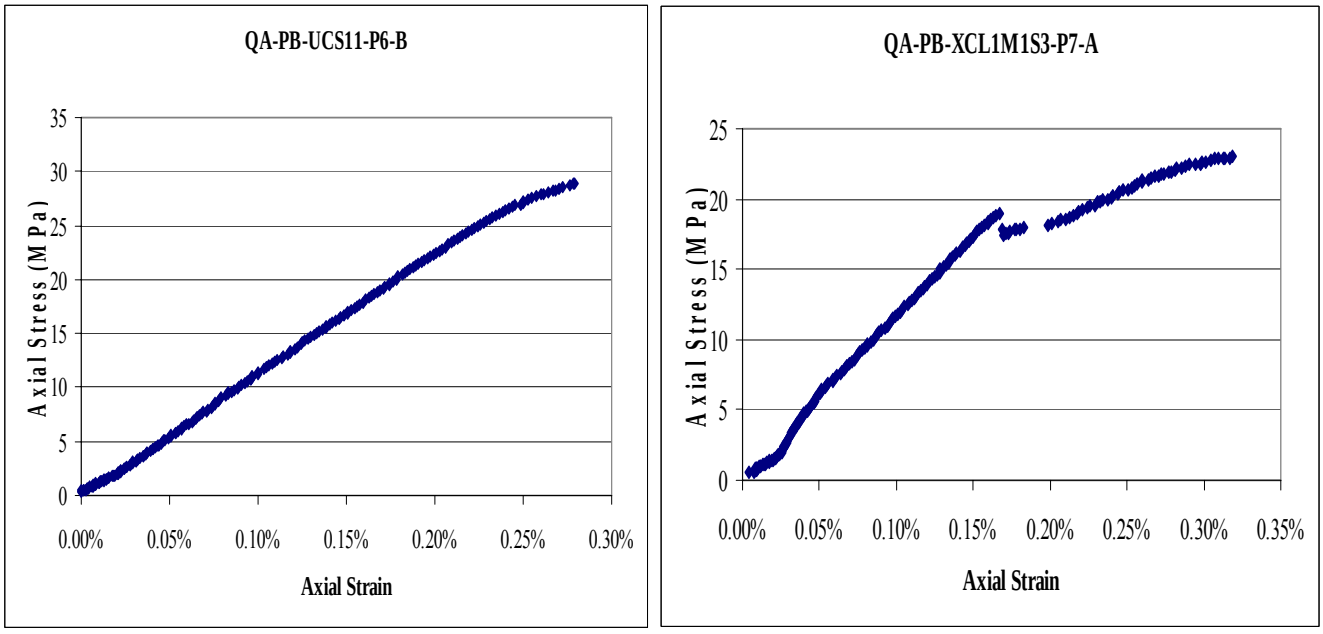

Source: Stress-strain data for tests taken from two electronic files associated with UCCSN-UNLV-073 Vol. 2: QA-PB-UCS11-P6-B calculation.xls and QA-PB-XCL1M1S3-P7-A calculation.xls. Note: Strain units are in./in x 100 (percent strain). For information only, not to be used for quality-affecting work.

Figure 7-4. Experimental Stress-strain Curves for QA-PB-UCS11-P6-B and QA-PB-XCL1M1S3-P7-A (UQ)

During testing, a progression of cracking between holes was sometimes noted. Often during these instances of progressive cracking, one or more local (sudden but small) drops in applied load was observed before the applied stress recovered to higher stress levels (Figure 7-4). For specimen QA-PB-XCL1M1S3-P7-A, pictured in Figure 7-5, a first crack appeared between the large and medium-size holes at about 6.9 MPa. After significantly more loading was applied to the specimen, two new cracks appeared at 18.6 MPa, one from the right side of the large hole (left photo) down to the corner of the specimen and the other from the medium hole up to the small hole above it. At 22.1 MPa, two new cracks appeared involving the uppermost small hole: a crack off to the left and terminating in the solid part of the specimen (approximately where the flaking is visible) and the other down and to the left side of the middle hole. At 23.0 MPa ultimate failure occurred with 12 new cracks appearing in the specimen. The cracking pattern on the back side of specimens is typically very similar to that visible on the front due to the fact that the holes extend through the specimen (assumed plane strain condition).

Sudden instances of spalling was observed (and noted in the laboratory notebook sheets) in some holes during testing (see spall material in the holes of Figure 7-5). Spall was not seen in holes that never experienced a crack.

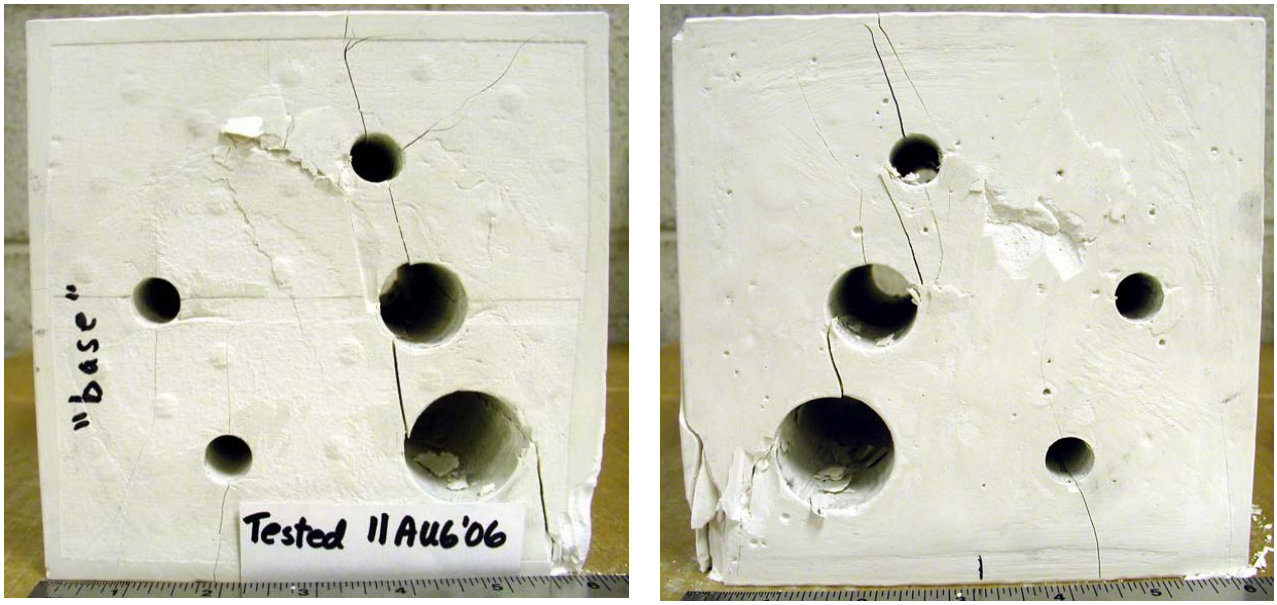

Figure 7-5. Post-test Failure Photos (front and back) of Specimen QA-PB-XCL1M1S3-P7-A

Local failure can be physically described as failure (cracking) in a portion of the specimen that is supporting a significant portion of load, possibly resulting in a substantial redistribution in stresses across the specimen. In these cases it was sometimes observed that an initial visible crack in one area would terminate growing larger and new cracks would appear in different areas of the specimen, due most likely to stress redistribution in the specimen after a local failure event. Some of the clearly visible initial cracks would also close up slightly (making them hard to see) as stress was relieved in this area of the specimen. As a result, it is sometimes difficult to ascertain all cracks in post-test photos (like Figure 7-5). Investigators may want to consult the sketches of all visible cracks that were prepared after each test as part of scientific notebook UCCSN-UNLV-073 Vol. 2.

The uniaxial compressive strength of a specimen represents the specimen failure strength for the purposes of this report, and is defined as that stress representing the peak or maximum uniaxial stress experienced by the specimen during its loading history. If progressive cracking was observed (usually just a few cracks), ultimate failure still happened relatively suddenly when many more cracks suddenly appeared (as described above for specimen QA-PB-XCL1M1S3-P7-A). For many specimens, only one or even no crack was noted before catastrophic failure of the sample occurred. For these specimens, the stress-strain response was relatively brittle. The sudden appearance of many cracks between holes and sides of the specimen was probably a consequence of the sudden release of a large amount of stored strain energy and initiated by a local failure (Figure 7-5 and 7-6). It is likely that failure occurred by progressive cracking occurring at a rapid rate to produce the final failure pattern with many cracks visible. Comparing solid and specimens with holes (lithophysal) behavior, the lithophysal specimen response tends to be less brittle since the holes allow for local failure and redistribution of stresses (to some degree) before peak failure is reached.

Specimen failure in terms of the final cracking pattern was characterized by a combination of tensile splitting and diagonal shear-type cracking across the specimen (Figure 7-5 and 7-6). Often a portion of the specimen and its holes had no visible cracks while other areas of the specimen experienced cracking connecting all or most holes. Failure in lithophysal specimens typically occurred over a range of 0.10 to 0.30 percent axial strain.

Summary. The observed uniaxial stress-strain behavior of specimens with holes was linear elastic up to a stress of about 75 percent of ultimate strength. Specimen failure is achieved by a series of local failures with progressive cracking between holes and edges of the specimen, but generally, most (and sometimes all) visible cracking occurs at the time of ultimate loading. The final failure pattern was typically a combination of tensile splitting and diagonal shear. A plane strain condition of specimens was noted with similar cracking patterns visible on both the front and back sides of specimens.

7.1.3 Behavior of Replicate Specimens

Each hole pattern was produced in triplicate and tested to failure. In general, the nature of cracking and final pattern of failure cracks was similar among the three replicate specimens. Two examples of patterns with replicate specimens are shown in Figure 7-6. Pattern QA-PB-UCL4-P13 specimens all show a vertical tensile crack from the top surface down to the left-most hole, shear cracking between neighboring holes towards the right, and a series of tensile cracks connecting the bottom surface to the holes above. The top right hole is not intersected by any cracks. In pattern QA-PB-UCS22-P12, the bottom right portion of each specimen has failed by tensile splitting and shear cracking between holes, while the top left portion of each specimen is crack free. More examples of this similar replicate behavior can be seen in Figure 7-9 and Appendix C.

The mechanical properties of replicate specimens were also similar. Typically, the standard deviation of Young's modulus values for the group of three replicates is around 1 to 2 GPa and about 1 to 2 MPa for ultimate strength values. The specimens shown in Figure 7-6 (and in Appendix C) demonstrate this trend. Note that in the Figure, the individual (and average) modulus and strength values for each specimen appear above the specimen photos.

Summary. The replicate specimen tests generally yielded similar patterns of failure (both in location and number of progressive cracks and final cracking patterns). Replicate tests also had relatively similar values of strength and modulus.

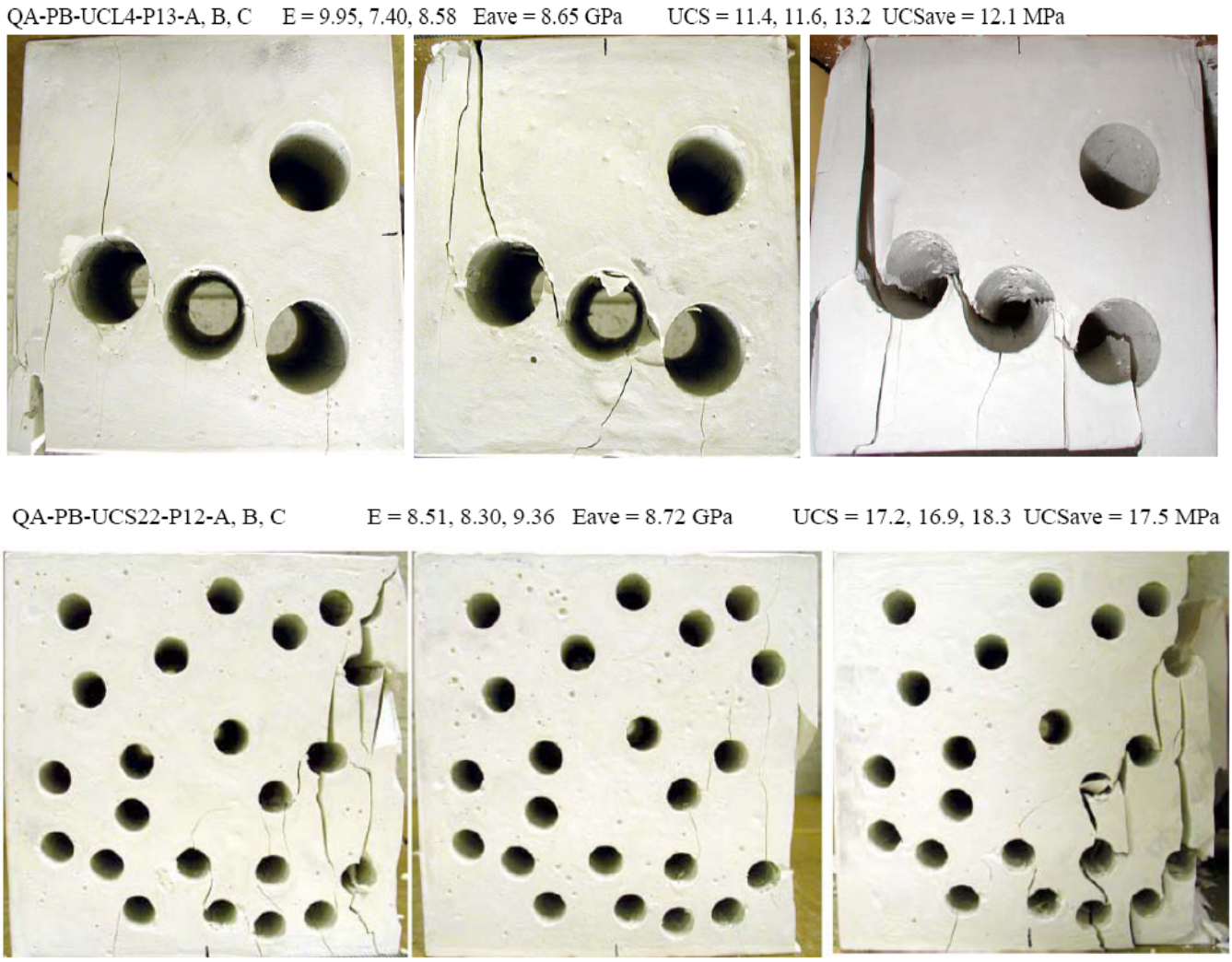

Source: Replicate E and UCS values come from scientific notebook UCCSN-UNLV-073 Vol. 2; worksheet "Data" in file "HydroStone Uniaxial and Porosity Data.xls." Eave and UCSave values come from DID 013DR.002, worksheet "QA Data Summary" or worksheet "QA Data Summary" in file "HydroStone Uniaxial and Porosity Data.xls." For information only, not to be used for quality-affecting work.

Note: E is Best fit Young's modulus, Eave is the average E, UCS is the uniaxial compressive strength, UCSave is the average UCS. The side view of specimens is shown: the top and bottom were the bearing surfaces for testing. For specimen QA-PB-UCS22-P12-B, the cracks are not very visible in the photo; however, the cracking pattern is similar to specimens A and C.

Figure 7-6. Photos of Replicate Specimens After Testing (UQ)

7.1.4 Mechanical Property Relationships

General Discussion.

Both of the pattern types shown in Figure 7-6 have approximately the same void porosity, 13 percent for the large hole pattern and 12 percent for the small hole pattern. Since void porosity has been proposed to be the primary physical property used to predict mechanical properties, similar values of average modulus (E) and strength (UCS) are expected, even though the geometrical pattern of voids and sizes of holes in the two patterns are quite different. The average E values of the two patterns are very close, 8.65 GPa and 8.72 GPa, respectively (Figure 7-6). The average UCS values of 12.1 MPa and 17.5 MPa (Figure 7-6) are about one standard deviation from the tabulated average value of 15.1 for 13% void porosity specimens (Table 7-2). In Section 7.1.5 it will be seen that smaller hole specimens yield higher strengths than larger hole specimens of similar porosity.

Table 7-2 presents a summary of all (all size and shape holes) analog rock specimen results grouped by void porosity (test results from pattern types A, B, and C are combined). These results confirm the expected result that Young's modulus and ultimate strength decrease systematically with increasing void porosity. From the solid specimen E of 16 GPa, there is a 31 and 46 percent drop in E value at 7 and 19 percent void porosity. From the solid specimen UCS of 55 MPa, there is a 60 and 82 percent drop in UCS value at 7 and 19 percent void porosity (Tables 7-1 and 7-2).

The standard deviations of these properties (Table 7-2) reflect the fact that there is more scatter in strength (UCS) values than elastic modulus (E) values (Tables 7-3 and 7-4, presented later, will also document this fact). As discussed earlier, the majority of specimens do not experience their first visible crack until a stress is reached that is more than 50% of the specimen's ultimate strength. Since the E values reported in Table 7-2 and Figure 7-7 are determined between the values of 25% and 50% ultimate strength, little or no cracking occurred to influence the elastic property results. Strength (UCS) is fundamentally different from E in that strength is determined well beyond the elastic range after significant specimen damage has occurred. Accordingly, it is likely that the higher standard deviation of UCS values is a consequence of the progression of cracking and changing stress distributions in specimens prior to failure.

Table 7-2: Mechanical Properties Summarized by Void Porosity

Porosity Groups	No. of Patterns	Ave. Void Porosity	Best Fit E (GPa)	E Stan. Deviation	UCS (MPa)	UCS Stan. Deviation
P6, P7	20	7 %	11.0	1.0	22.3	3.2
P12, P13, P15	20	13 %	9.9	1.6	15.1	2.5
P18, P19, P20	12	19 %	8.6	1.4	9.9	2.1

Source: Data comes from 013DR.002; worksheet "Data by porosity".

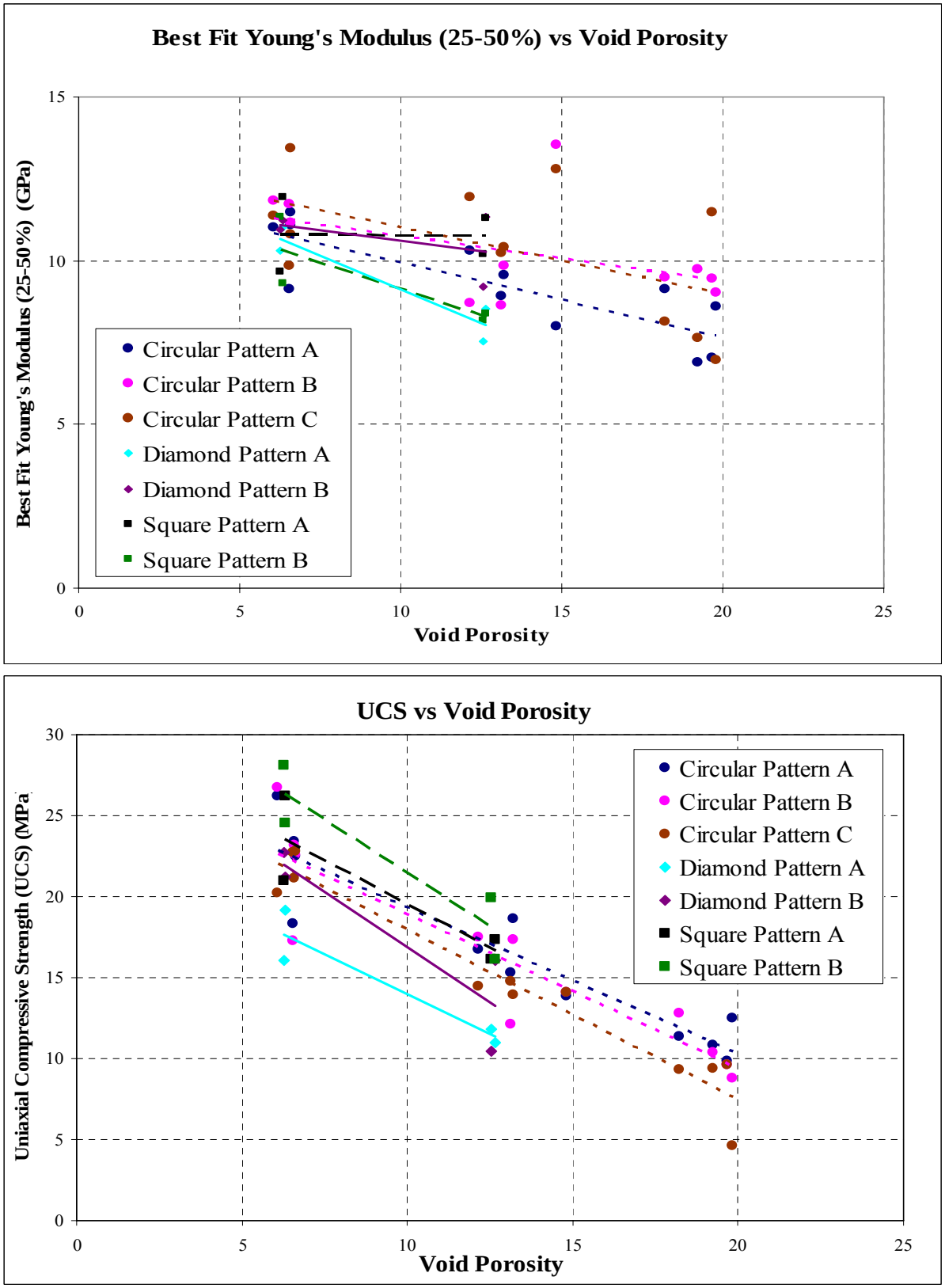

Source: Plot data comes from 013DR.002; worksheet "Plots". The trend lines shown in the plots are linear.

Figure 7-7. Variation in Young's Modulus (top) and UCS as a Function of Void Porosity

Both the relationship between Young's modulus with void porosity and strength with void porosity is roughly linear (see Figure 7-7). The average "R^2" value (coefficient of determination) of the best-fit linear trend lines shown in Figure 7-7 is 0.43 with a standard deviation of 0.32 for the Young's modulus plot and 0.83 with a standard deviation of 0.04 for the trend lines in the strength plot (DID 013DR.002, worksheet "Plots"). The higher coefficient of determination value for strength and void porosity is a reflection of the fact that higher void porosity impacts strength more than modulus. The observed linear dependence of mechanical properties on void porosity is valid for specimens with a void porosity ranging from about 5 to 20 percent (the lower and upper limits of this research). If the linear trend is extrapolated to zero void porosity, a modulus of about 13 GPa and strength of 30 MPa is predicted. However, since the solid specimen properties are 16 GPa and 55 MPa (Table 7-1), the observed linear relationship does not hold over the zero to 5 percent range.

The relationship between uniaxial strength and elastic modulus is plotted in Figure 7-8. The figure illustrates that modulus correlates positively to uniaxial strength in a linear manner, but the fit involves a significant amount of scatter.

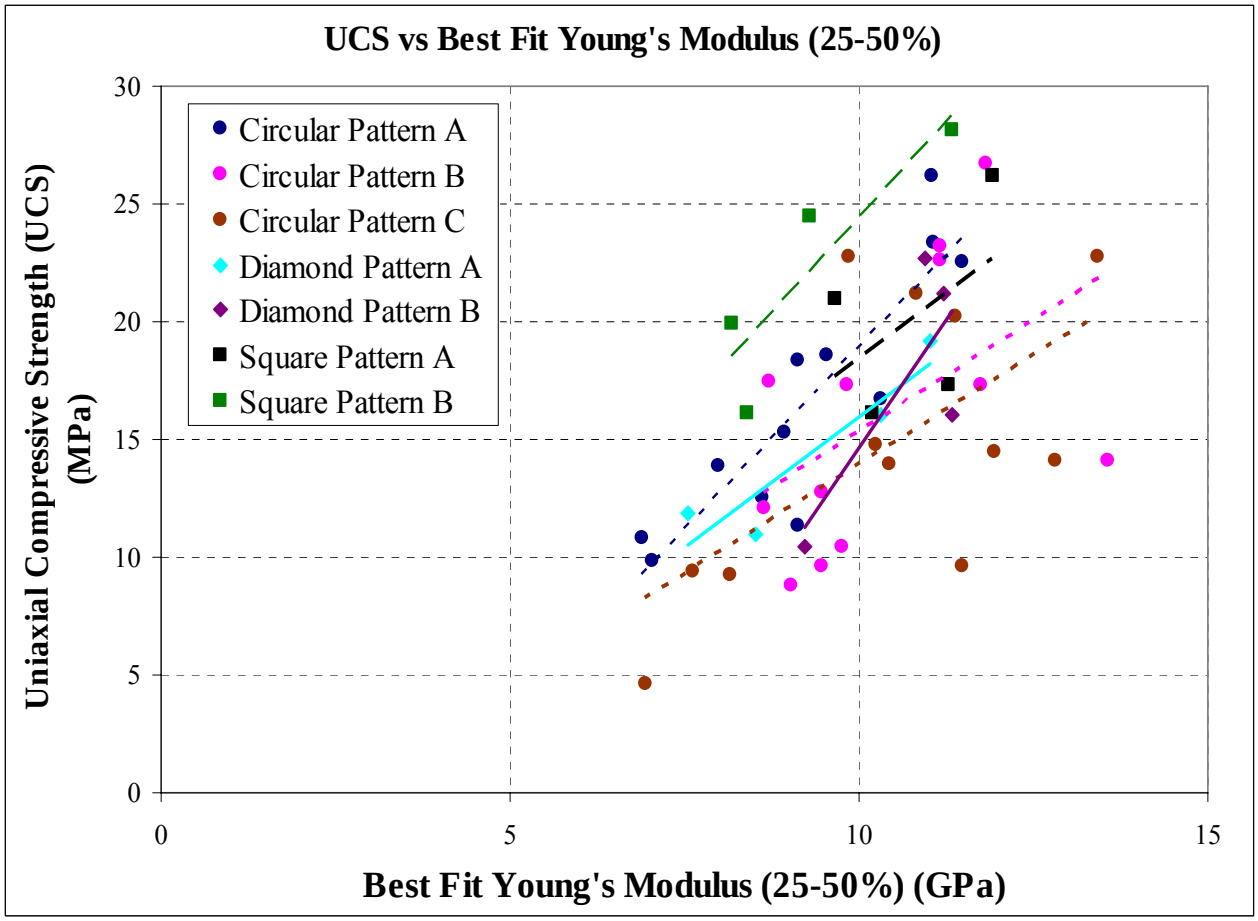

Source: Plot data comes from 013DR.002; worksheet "Plots". The trend lines shown in the plot are linear.

Figure 7-8. Variation in Uniaxial Compressive Strength with Best Fit Young's Modulus

As discussed earlier, Patterns A, B, and C represent different randomly generated hole geometries. Grouped test results by pattern type is shown in Figure 7-7, Table 7-3, and in further plots found in DID 013DR.002, worksheets "Pattern A", "Pattern B", and "Pattern C". Examining the plots and statistics of these results, it is apparent thatYoung's modulus and strength values for each of the three patterns yield similar results (similar mean values that are well within the associated standard deviations) and trends of behavior (decreasing property values with increasing void porosity). No property dependency based on pattern type could be identified. As a result, statistical summaries and plots in this report generally combine pattern A, B, and C results.

Table 7-3: Comparison of Results from Patterns A, B, and C

Pattern Type	No. of Patterns	Best Fit E (GPa)	BF S.D.	UCS (MPa)	UCS S.D.
A	12	9.3	1.5	16.6	5.3
B	12	10.4	1.5	16.0	5.8
C	12	10.4	2.0	14.8	5.9

Source: Data comes from 013DR.002; see worksheet "All data".

Note: "Best Fit" is 25 to 50% best fit Young's modulus, "BF" is best fit, "S.D." is standard deviation, "UCS" is the uniaxial compressive strength. Hole size and shape data is combined.

Summary. The Hydro-Stone TB® uniaxial experimental results show that as void porosity increases, both the Young's modulus and ultimate strength values decrease. The void porosity is the primary physical property useful for predicting mechanical properties, more significant than size of hole or shape of hole. At similar void porosities, there is higher scatter in strength results than for Young's modulus values. The modulus and strength with void porosity relationships are essentially linear over the 5 to 20 percent void porosity range; this relationship does not hold when zero void porosity (solid specimen) results are considered. From solid specimens there is roughly a 60 percent drop in strength with about 7 percent void porosity, increasing to approximately an 80 percent drop at 19 percent void porosity. The percent change in modulus from the solid specimen value is roughly 30 and 45 percent at 7 and 19 percent void porosity, respectively. So, the loss in strength is significantly greater than the decrease in modulus for similar increases in porosity. A linear relationship exists between modulus and strength, although a fair amount of scatter is seen. Patterns A, B, and C in this research each give basically the same statistical trends and result.

7.1.5 Effect of Hole Size on Mechanical Properties

General Discussion. The experimental plan was designed to study the effect of hole size on mechanical properties. For each of the basic hole patterns (A, B, and C), target porosities were created using only small holes, only medium-sized holes or only large holes. Specimens were also produced that combined different size holes and targeted certain void porosities. After uniaxial testing, the small-, medium-, large- and mixed-size circular hole data was plotted separately by pattern type (DID 013DR.002, worksheets "Pattern A", "Pattern B", and "Pattern C").

Young's Modulus. Overall, plots of best fit Young's modulus vs. void porosity showed no discernable dependence on void size; almost all the data in the plots overlapped each other except for Pattern A where large hole specimens had the lowest values. Table 7-4 summarizes the statistics of circular A, B, and C pattern specimens grouped by hole size. This data shows essentially the same average value of Young's modulus. In worksheet "Data by Porosity" (DID 013DR.002), the experimental results summarized in Table 7-4 are broken down further into porosity groups. Again, no clear dependence between Young's modulus and size of void was found.

Uniaxial Strength. Plots of strength vs. void porosity in patterns A and B showed a slight dependence on size: at similar void porosities, smaller hole specimens had slightly higher strengths than larger hole specimens. For pattern C no size dependence was evident; all the plots overlapped each other. The mixed size hole specimen results plotted in between the small and large hole data. The Table 7-4 summary of data also illustrates a possible correlation between smaller size specimen holes and increasing strength. Breaking the Table 7-4 data into porosity groups, the same overall trend is evident (Table 7-5). This effect could be due to the average specimen bridge lengths being larger in smaller hole specimens.

Summary. No dependence of Young's modulus on void hole size is discernable. There may be a slight dependence of uniaxial strength on void hole size; smaller hole specimens tend to have higher strengths.

Table 7-4: Mechanical Property Dependence on Void Hole Size

Pattern Type	No. of Patterns	Best Fit E (GPa)	BF S.D.	UCS (MPa)	UCS S.D.
Large	9	9.6	1.4	14.4	4.6
Medium	9	10.1	1.9	16.0	6.5
Small	9	10.2	1.4	17.3	6.2

Source: Data comes from 013DR.002; see worksheet "Data by Porosity".

Note: "Best Fit" is 25 to 50% best fit Young's modulus, "BF" is best fit, "S.D." is standard deviation, "UCS" is the uniaxial compressive strength. Similar porosity and pattern A,B,C data is combined. The relatively large standard deviations are due to values included from various porosities. When data is further segregated into porosity groups (3 patterns each), the same general trend is evident (see worksheet "Data by Porosity", "013DR.002").

Table 7-5: Ultimate Strength Dependence on Void Hole Size

Porosity Groups	No. of Patterns	Large UCS (MPa)	Large S.D.	Medium UCS (MPa)	Medium S.D.	Small UCS (MPa)	Small S. D.
P6, P7	3	19.5	2.9	22.6	0.1	24.4	3.6
P12, P13	3	14.0	1.7	16.6	2.4	16.2	1.6
P18, P19, P20	3	9.7	0.1	8.6	4.0	11.1	1.8

Source: Data comes from 013DR.002; see worksheet "Data by Porosity".

Note: "UCS" is the uniaxial compressive strength, "S.D." is standard deviation. Similar porosity and pattern A,B,C data is combined.

7.1.6 Effect of Void Shape on Mechanical Properties

General Discussion. An imaginary long and thin rectangular hole oriented perpendicular to the axis of compression (horizontally) would greatly reduce modulus and strength values of a specimen. The same rectangular hole oriented parallel to the axis of compression (vertically) would not have a great effect. For this research it was decided to study the effect of no corners (circles) and corners with differing orientation (squares and diamonds). Hole shapes were chosen that were symmetrical both horizontally and vertically to minimize the effect noted earlier in this paragraph.

Returning to Figure 7-7, it appears that hole shape does not influence elastic modulus values, but does have an impact on specimen strength. In this figure, circle markers are used for specimens with circular holes, square markers for square holes, and diamond markers for diamond holes. Two pattern types (A and B) were used for square and diamond hole specimens. To help further distinguish between specimen data on plots, dotted trend lines are used to represent the best linear-fit to the circular-hole data, dashed trend lines for square holes, and solid lines for diamond-shaped holes. Since size of hole has only slight or no effect on mechanical properties in this research (Section 7.1.5), void size is ignored as a variable of interest in examining the effect of void shape.

Young's Modulus. In the modulus vs. porosity plot (Figure 7-7, top), it can be seen that most of the data points are bunched in the same range of modulus for a given porosity value, the various shape trend-lines tend to overlap, and there seems to be a significant amount of scatter in results. Statistics on the trend lines confirm this latter observation as the average "R^2" is 0.43 with a standard deviation of 0.32 (DID 013DR.002, worksheet "Plots"). Hole shape comparisons broken down by pattern type can be seen in worksheets "Pattern A" and "Pattern B", and these yield the same non-significant result. Consequently, hole shape is deemed to be insignificant to modulus.

Uniaxial Strength. The plot of strength versus void porosity (Figure 7-7, bottom), appears to show a dependence on hole shape. In the plot the points seem bunched according to shape (squares highest, diamonds lowest). Both of the square trend lines plot higher than the three circular-hole trend lines, which, in turn, plot higher than both diamond trend lines. Finally, there is relatively little scatter or overlap between specimens of different shape holes. Statistics on the trend lines confirm this latter point as the average "R^2" is 0.83 with a standard deviation of 0.04 (DID 013DR.002, worksheet "Plots"). Hole shape plot comparisons broken down by pattern type can be seen in worksheets "Pattern A" and "Pattern B". For both of these patterns large and small square holes have higher strengths than any diamond holes. Accordingly, all other things being equal, the square hole specimens have the highest strength, diamond-shaped holes give the minimum strength, and circular holes have an in-between strength. We have already noted that squares and diamond both have sharp corners, whereas circles do not, so what accounts for the shape effect?

Itasca Consulting Group authored a numerical shape study (Rigby, D.B. 2004, Section 6.5.4) and proposed that the average length of solid material between holes may be an important predictor of strength. As part of this experimental research, square, diamond, and circular shape holes were molded into identical geometrical locations within specimens (one pattern is shown in Figure 7-9). Diamond holes were all placed in an orientation such that their points lined up with the vertical and horizontal, and squares were always lined up with their sides parallel to the sides of the specimen. Considering a hypothetical uniform patterning of holes where the centers of diamonds, squares, and circles line up vertically and horizontally, it is obvious that diamond-hole patterns would produce the shortest distance between hole corners (shortest bridge length) and square-hole patterns the longest bridge lengths. Since the diameter of an equivalent area circle is between the height of a square and diamond, then similarly located pattern of circular holes should have an average bridge length between that of diamond and square-hole specimens.

As previously noted, hole patterns were generated by successively locating additional holes at random. Even with this more random geometry, Figure 7-9 appears to show that square-hole bridge lengths tend to be longer than diamond-hole bridge lengths, meaning that higher stress concentrations may exist in diamond-hole specimen bridge material. Some of the cracks are hard to see in the figure, but generally hole-to-hole cracking occurs by tensile splits or by diagonal shear, often initiating and ending at sharp corners (not the shortest distance between holes). In addition, the diamond shape and orientation may be more conducive to initiation of the typical vertical tensile splitting that is observed. Thus it may follow from these two factors that, on the average, cracks will likely form earlier in the diamond hole specimens, and may result in a smaller ultimate failure stresses. Given the square and diamond hole configurations of this research, circular hole geometry and specimen behavior could be expected to lie somewhere in between that of square and diamond hole specimens. This is a qualitative assessment that could be confirmed by quantitative measurements and numerical modeling.

QA-PB-USqL6-P13-A, B, C E = 8.07, 8.03, 8.43 Eave = 8.18 GPa UCS = 20.2, 19.1, 20.4 UCSave = 19.9 MPa

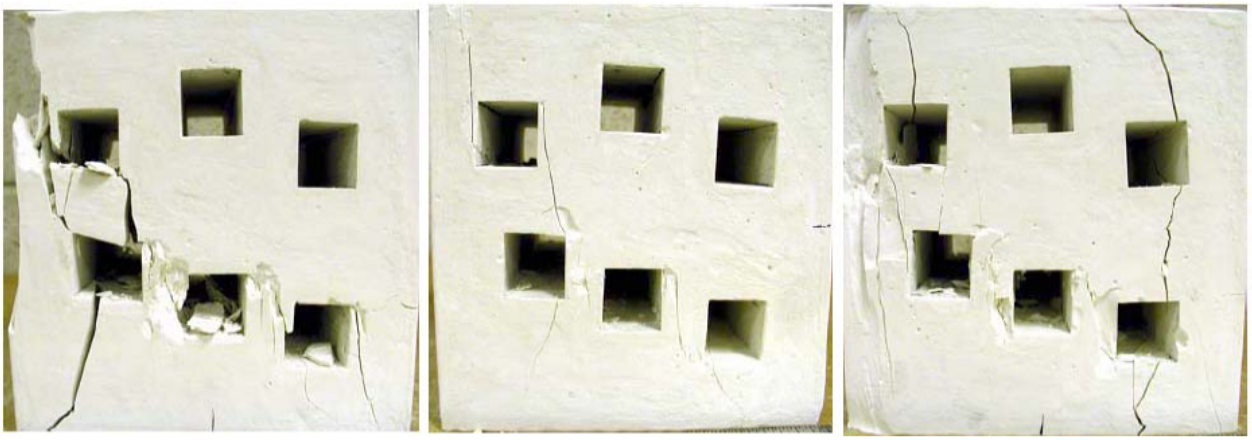

QA-PB-UDmL6-P13-A, B, C E = 10.3, 7.62, 9.69 Eave = 9.22 GPa UCS = 9.9, 10.4, 11.1 UCSave = 10.5 MPa

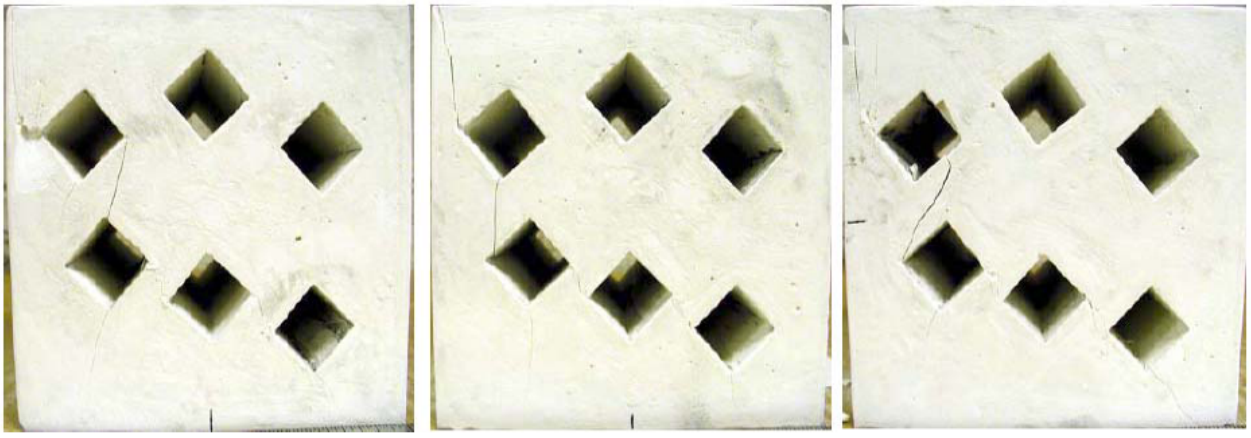

Source: Replicate E and UCS values come from scientific notebook UCCSN-UNLV-073 Vol. 2; worksheet "Data" in file "HydroStone Uniaxial and Porosity Data.xls." Eave and UCSave values come from DID 013DR.002, worksheet "QA Data Summary" or worksheet "QA Data Summary" in file "HydroStone Uniaxial and Porosity Data.xls." For information only, not to be used for quality-affecting work.

Note: E is Young's modulus, Eave is the average E, UCS is the uniaxial compressive strength, UCSave is the average UCS.

Figure 7-9. Replicate Specimens with Square- and Diamond-Shaped Holes (UQ)

Summary. The experimental data showed no dependence of Young's modulus on void hole shape (at similar values of porosity), but a moderate correlation between strength and void shape. It is likely that the shape dependence is related to both orientation of the shapes and average bridge length.

7.1.7 Normalized Plots of Mechanical Behavior

General Discussion. It may be useful to normalize the experimental results plotted in Figures 7-7 and 7-8. In the previous Task 27 research (Avar 2003; Avar, et. al. 2003; and Hudyma, et. al. 2004), normalization was used to compare trends among the different materials tested (rock and plaster of Paris). Even though rock is much stiffer and stronger than plaster of Paris, the normalized modulus and strength results from these materials essentially plotted on top of each other. For this research, normalization was accomplished by dividing the various values of modulus and strength determined from tests on specimens with holes by the average solid specimen values. Figures 7-10 to 7-12 are the normalized plots of the experimental results, not distinguishing shape or size of hole. Since the Yucca Mountain project reports have traditionally fit an exponential curve to experimental and numerical properties with void porosity, a best-fit exponential trend line (black) is included in Figures 7-10 and 7-11. A linear fit is used in Figure 7-12, again in conformance with project reports.

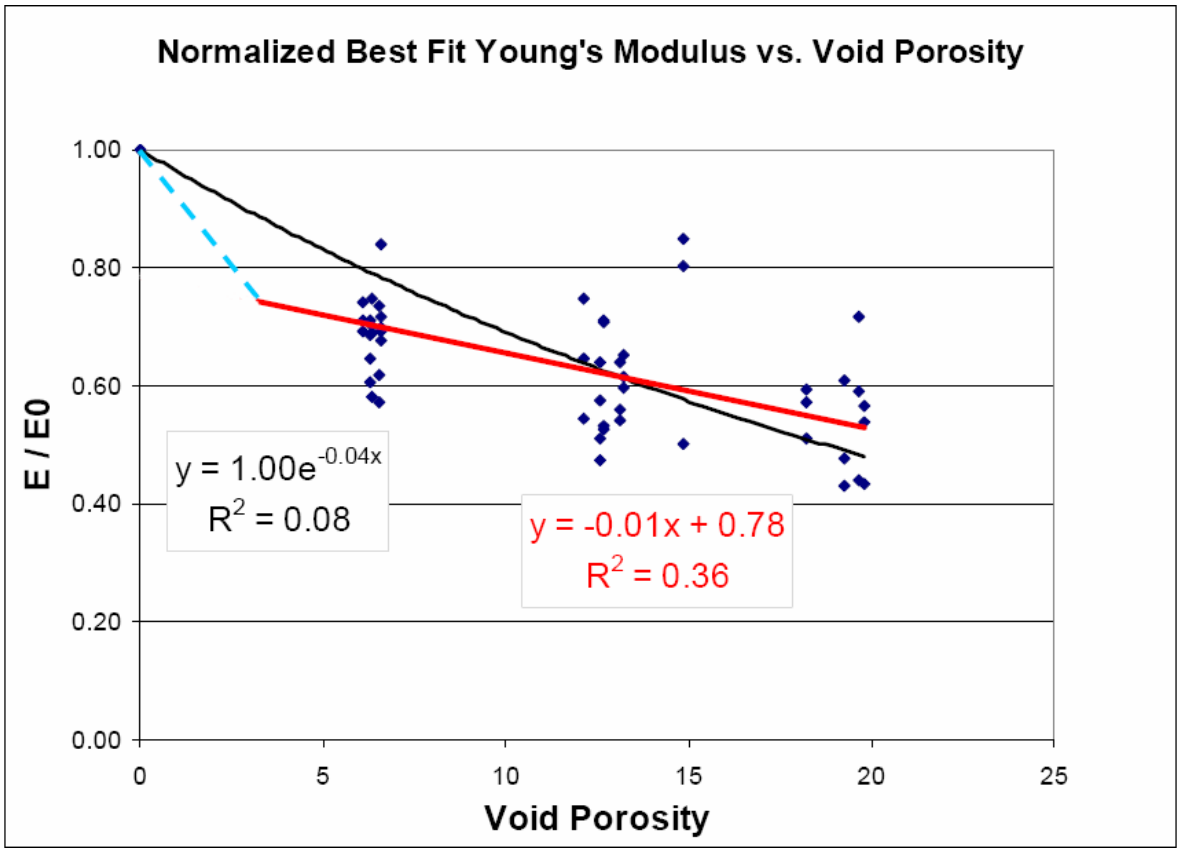

Source: DID 013DR.002; worksheet "Plots".

Note: Black trend line is exponential best-fit through 1.00, red is linear best-fit to data, blue dashed line intersects the red line at an arbitrary (unknown) small value of porosity. Blue and red lines represent a possible bilinear model.

Figure 7-10. Relationship between Normalized Young's Modulus and Void Porosity

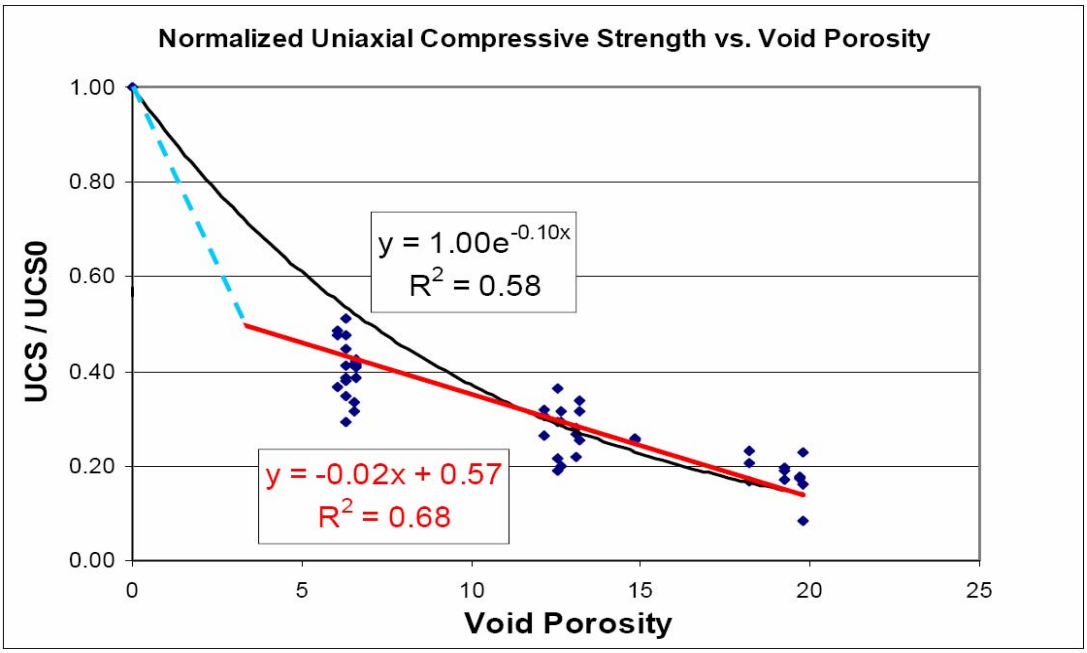

Source: DID 013DR.002; worksheet "Plots".

Note: Black trend line is exponential best-fit through 1.00, red is linear best-fit to data, blue dashed line intersects the red line at an arbitrary (unknown) small value of porosity. Blue and red lines represent a possible bilinear model.

Figure 7-11. Relationship between Normalized Uniaxial Compressive Strength and Void Porosity

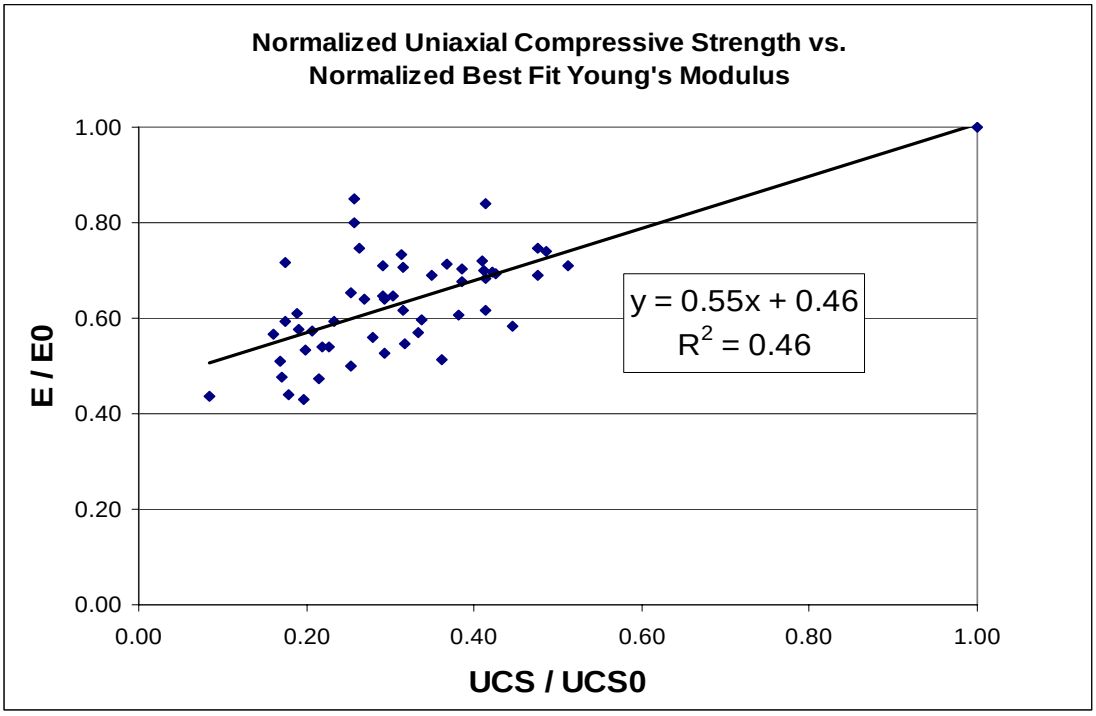

Source: DID 013DR.002; worksheet "Plots".

Figure 7-12. Relationship between Normalized UCS and Young's Modulus

Figures 7-10 and 7-11 show that the steep reduction in modulus and strength values that occurs upon moving from solid specimens to specimens with voids is not well represented by an exponential fit. The normalized Young's modulus versus porosity exponential fit curve (Figure 7-10) doesn't model the data relationship well at all; R^2 is 0.08. The normalized strength versus modulus versus porosity data fits an exponential curve slightly better but still is not a good fit (Figure 7-11); R^2 is 0.58. For both cases almost all the data grouped at about 7% void porosity plots below the respective exponential best-fit line.

As discussed in Section 7.1.4, the relationship between Young's modulus with void porosity and strength with void porosity is roughly linear (see Figure 7-7). A better fit to the data may be bilinear fit (dashed blue and red lines) shown in Figures 7-10 and 7-11. The coefficient of determination of the best-fit linear trend lines is better than for the exponential fit, but is still not good due to the amount of scatter present within each of the porosity groupings (Figures 7-10 and 7-11). However, visually the linear models fit the center of the data groups quite well. The problem for the bilinear model is knowing at what point (void porosity) the dashed blue line should intersect the red line since there is no available data between zero and 7 percent porosity.

Summary. An exponential curve is not a good fit to the normalized experimental data (modulus and strength with void porosity). A bilinear model gives a much better fit to the normalized data.

7.1.8 Young's Modulus Methods of Determination

General Discussion. For all specimens tested, three methods of determining Young's modulus were carried out: tangent value at 50% of ultimate strength, secant determined from 0 to 50% ultimate strength, and best fit value over the range of 25% to 50% ultimate strength. Generally, for these reported values, the tangent value consistently provides the highest modulus, best fit is in the middle and the secant provides the lowest value of Young's modulus. This relationship can be seen in the "Modulus Type Comparison" plots found in DID 013DR.002, worksheets "Pattern A", "Pattern B", and "Pattern C" and in Table 7.6.

Table 7-6: Comparison of Various Methods to Determine Young's Modulus

Porosity Groups	No. of Patterns	Ave. Void Porosity	Tangent E (GPa)	Tan S.D.	Best Fit E (GPa)	BF S.D.	Secant E (GPa)	Sec S.D.
P6, P7	20	7 %	12.0	1.7	11.0	1.0	10.1	2.0
P12, P13, P15	20	13 %	10.7	2.6	9.9	1.6	8.6	2.5
P18, P19, P20	12	19 %	9.5	2.6	8.6	1.4	6.2	1.4

Source: DID 013DR.002; worksheet "Data by Porosity".

Note: "Tangent" is 50% tangent Young's modulus, "Tan" is tangent, "Best Fit" is 25 to 50% best fit Young's modulus, "BF" is best fit, "Secant" is 0 to 50% secant Young's modulus, "Sec" is secant, "S.D." is standard deviation. Hole size and shape as well as pattern A,B,C data is combined.

Best Fit Young's Modulus (25-50% strength) is recommended to be used in preference to other reported E values. This is based on: (1) the 25-50% range of ultimate strength tends to be the most linear part of stress-strain curve, (2) the tangent and secant derived E values are based on one or two data points only that are susceptible to local variations in slope, and (3) the best-fit determination of E is determined by using many data points.

Summary. Young's modulus determinations resulted in tangent at 50% having the highest value, best fit over 25 to 50% giving an intermediate value, and the 0 to 50% secant value giving the lowest Young's modulus. It is recommended that the best fit Young's modulus (25 to 50%) be used.

7.1.9 Validation of Yucca Mountain Numerical Models (UQ)

Importance. As discussed in Section 4.2, the specific influence of void geometry (shape, size, and distribution) on mechanical properties has been predicted by numerical models, but these predictions have not been validated by experimental testing. A good first step of validation would be to ensure that the numerical models can reproduce the behavior of laboratory specimens of a given known geometry of heterogeneity. This research is limited to the uniaxial compression testing of such analog lithophysal rock specimens. Subsequent validation efforts could focus on different load paths (e.g., tensile) and different (larger) specimen scales.

An approach of bounding conservatism has been adopted by the project, but these assumptions are based in part on correct predictions from PFC and UDEC numerical models. I am not aware that any of these models have been calibrated and validated for specific specimens of lithophysal rock. The prior calibration approach was limited to adopting expert-judgment based values of the strength and modulus of lithophysal rock mass. And to date, validation has consisted of behavioral comparisons with a number of large-core specimens of lithophysal rock (of uncertain heterogeneity) and with the general condition of drift tunnels passing through lithophysal rock.

A cut in funding for this project eliminated the QA subtask to calibrate UDEC to the observed behavior of solid analog rock and then use UDEC to predict the behavior of specific geometries of analog rock under simulated uniaxial testing. However, it was deemed useful to the project to (1) compare the observed behavior of the analog lithophysal rock to specific patterns of behavior observed in project numerical modeling, and (2) overlay the new analog rock results on previously plotted results including both numerical predictions and actual lithophysal rock specimens. Discussions of these activities follow.

Discussion of Compared Results. The general experimental stress-strain response observed in the uniaxial testing of the Hydro-StoneTB® rock specimens as well as the nature of specimen failure (as described in Section 7.1.2) is very similar to that described for the PFC and UDEC computational models (Rigby, D.B. 2004, Section 6.5.4, p. 6-74). In the numerical models, adding macro-size voids resulted in significant decreases in both the peak strength and Young's modulus. The numerical failure mechanism seen in simulated tests was generally described as tensile failures of local bridge material connecting adjacent voids. These resulted in a progressive failure of the specimen along directions conducive to shear and/or vertical tensile splitting Overall, the numerical stress-strain response was characterized as being brittle. In sum, the nature and manner of failure of the experimental tests confirmed the behavior of the numerical models.

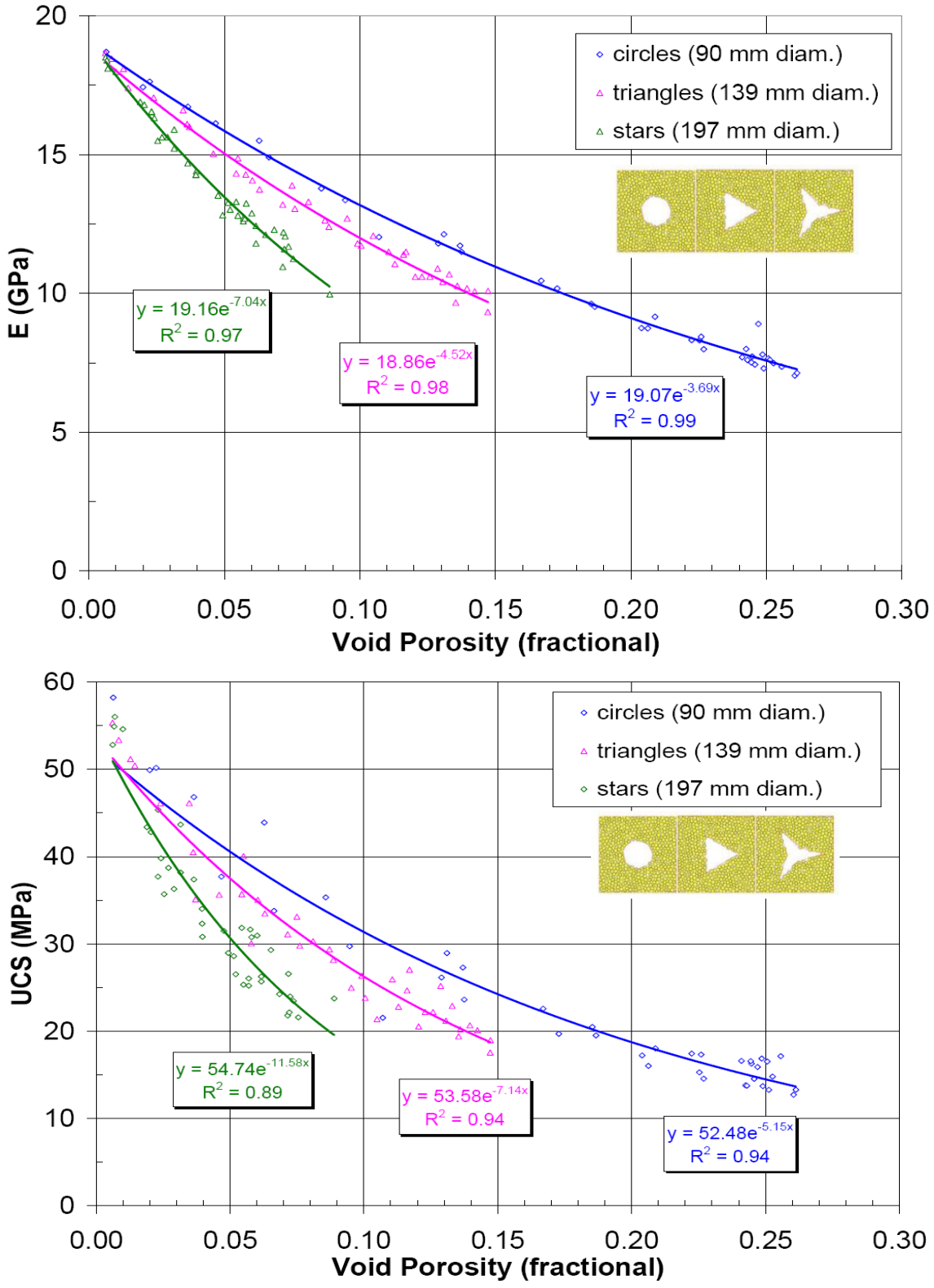

Source: Scientific Notebook UCCSN-UNLV-073 Vol. 2, Attachment H, "ShapeStudy_UNLV_Task13.xls", worksheets "E(c-t-s)" and "qu(c-t-s)". For information only, not to be used for quality-affecting work.

Figure 7-13. PFC2D Numerical Study Predicting Affect of Void Shape on Mechanical Properties (UQ)

The effect of void shape on mechanical properties was studied numerically by simulating uniaxial compressive tests using PFC2D models with voids (Rigby, D.B. 2004, Section 6.5.4). Three constant-size hole shapes (circles, triangles and stars) were placed in random locations and orientations in numerical models. The numerical study predicted that void shape significantly affected Young's modulus (Figure 7-13, E vs. Void Porosity plot). For similar values of void porosity, circular hole specimens gave the most stiff response, triangle hole specimens a less stiff response, and star-shaped voids resulted in the least stiff behavior. As discussed in Section 7.1.6, the present experimental study does not validate the claim that hole shape is significant to Young's modulus values. This experimental result appears to make theoretical sense as long as (1) the total area of holes is spread out approximately equally relative to both the horizontal and vertical axes, and (2) the stresses and strains in the specimen remain in the elastic range (both points appear to be valid for the numerical study).

The numerical study also predicted that void shape significantly affected uniaxial strength (Figure 7-13). The numerical model predicts that specimens with circular holes have the highest strength, triangular holes less strength and star-shaped holes the least strength (Figure 7-13, UCS vs. Void Porosity plot). Square-shaped holes were not modeled in the numerical study. As discussed in Section 7.1.6 of this report, the experimental testing confirmed a correlation between shape and specimen uniaxial strength. As can be seen in the plots, there is a relatively small amount of scatter about the trend line for the numerical models.

The numerical shape study was carried out using the PFC2D program. There may be numerical issues, specific to the PFC2D program, that affects model predictions. For instance, does the number of corners have an effect or do the constituent particles making up the model behave in a way that may be inconsistent with actual rock behavior? It would be instructive to carry out similar shape study predictions with the UDEC program to see if there are any differences in predictions.

Figures 7-14 and 7-15 show the normalized results from PFC numerical model predictions, large core lithophysal tuff experimental results and Hydro-StoneTB® experimental results. In Figure 7-14, the normalized modulus versus void porosity plot for the Hydro-StoneTB® specimens overlaps the PFC numerical predictions, but with more scatter apparent in the experimental data. In Figure 7-14, the normalized strength versus void porosity plot for the Hydro-StoneTB® specimens forms a lower bound to the PFC numerical predictions, again with a fair amount of scatter in the experimental data. Whereas the numerical model data follows an exponential fit, the experimental data appears to be modeled better by a simple bilinear fit (red lines in plots).

The numerical shape predictions tightly overlap each other along an exponential curve in a normalized plot of strength versus Young's modulus (Figure 7-15). The analog rock experimental data plots below the numerical predictions (primarily due to the lower normalized strength values) and are much more scattered than the numerical data. The same bilinear model (dashed and solid red lines) from Figure 7-14 are also plotted in Figure 7-15. For strength versus Young's modulus analog rock experimental data, the bilinear model is not much different than an exponential fit to the.data.

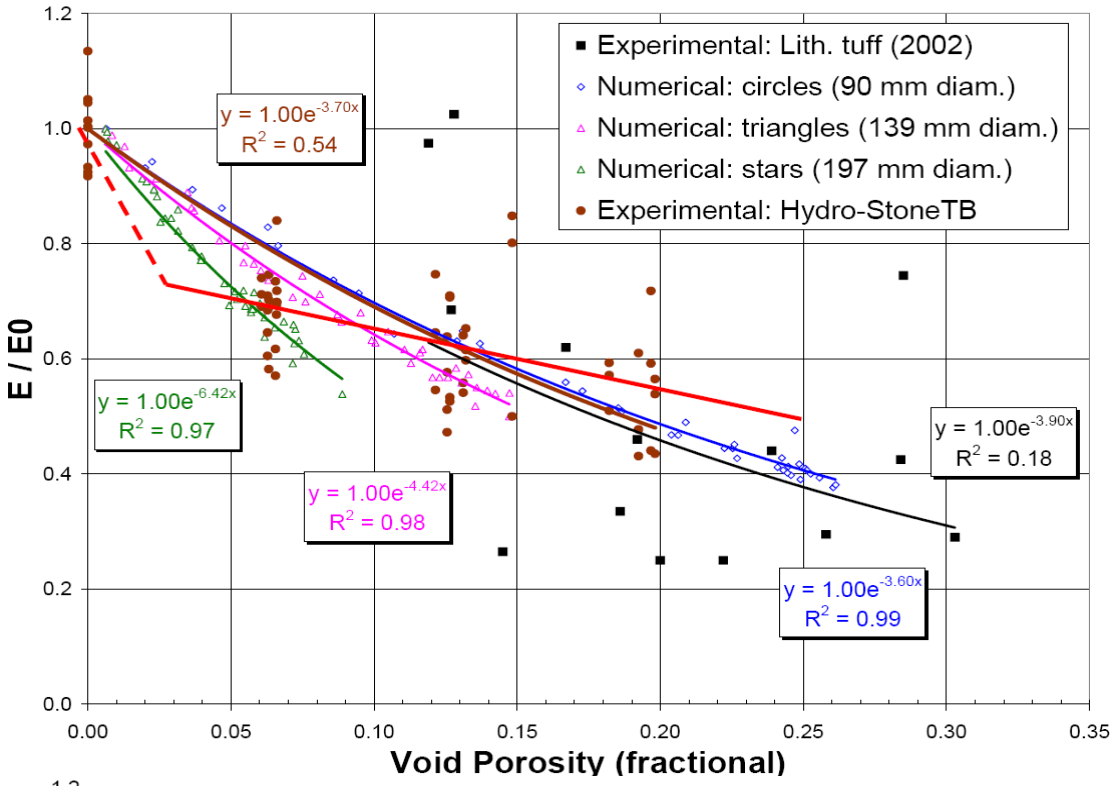

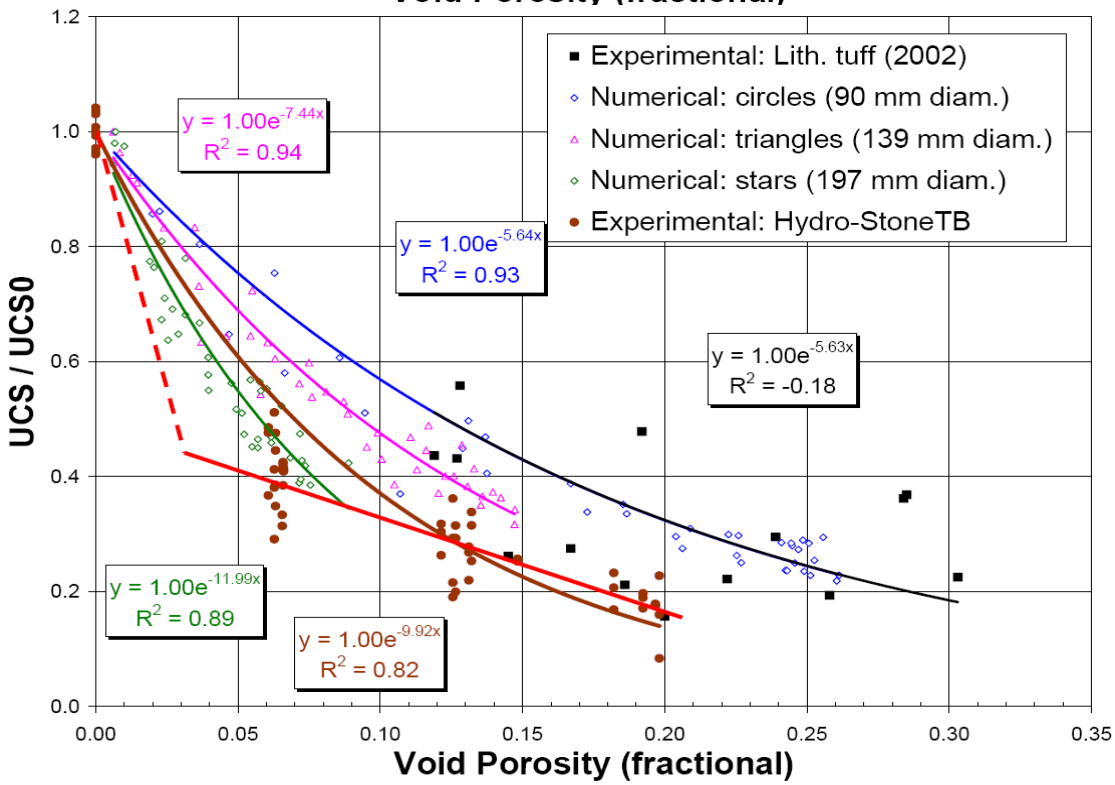

Source: Scientific Notebook UCCSN-UNLV-073 Vol. 2, Attachment H, "ShapeStudy_UNLV_Task13.xls", worksheets "E(c-t-s)-HS norm" and "qu(c-t-s-HS) norm". For comparative purposes only, not to be used for quality-affecting work.

Note: Dashed and solid red lines represent a possible bilinear model for fitting the Hydro-StoneTB® experimental data.

Figure 7-14. Normalized Numerical Predictions, Tuff and Analog Rock Results with Void Porosity (UQ)

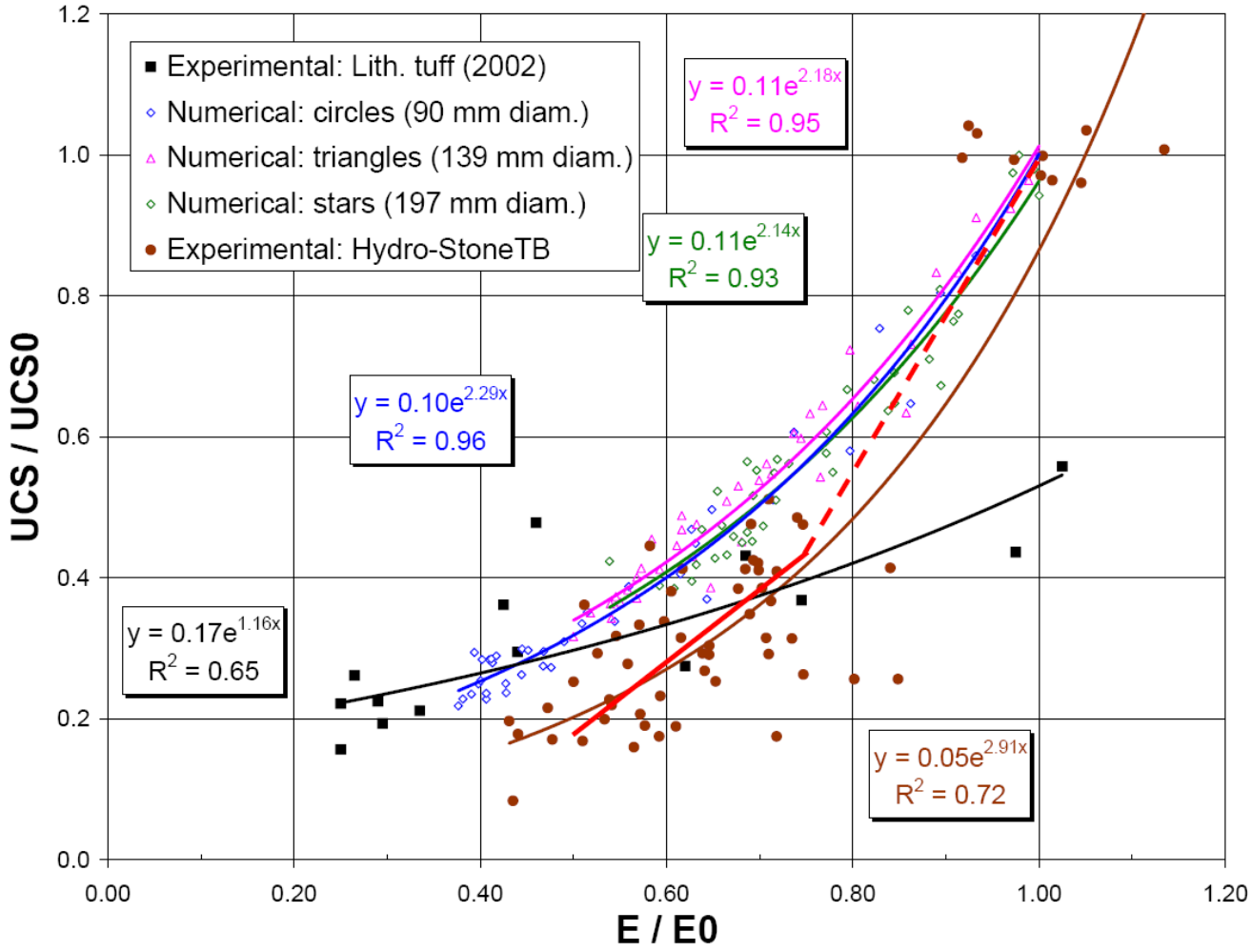

Source: Scientific Notebook UCCSN-UNLV-073 Vol. 2, Attachment H, "ShapeStudy_UNLV_Task13.xls", worksheet "E_qu(c-t-s) norm". For comparative purposes only, not to be used for quality-affecting work.

Note: Dashed and solid red lines represent a possible bilinear model for fitting the Hydro-StoneTB® experimental data.

Figure 7-15. PFC Numerical Predictions, Tuff and Analog Rock Results, UCS/UCS0 vs. E/E0 (UQ)

For bounding the mechanical properties of Topopah Spring lithophysal tuff, the project adopted upper and lower bounding curves (shown in red in Figures 7-16 and 7-17). These curves bound the uniaxial experimental tests on lithophysal tuff, the numerical shape study results and numerical predictions of uniaxial tests on large 1 m by 1 m "panel map" models with realistic geometries of Lithophysae (stenciled from actual 2D lithophysal maps and shown as crosses in the plots). When the Hydro-StoneTB® experimental test results are superposed on these plots (brown filled triangles in Figures 7-16 and 7-17), it is seen that the experimental data matches the "panel map" specimen numerical predictions quite closely, which exhibits lower strength than any of the numerical shape study results.

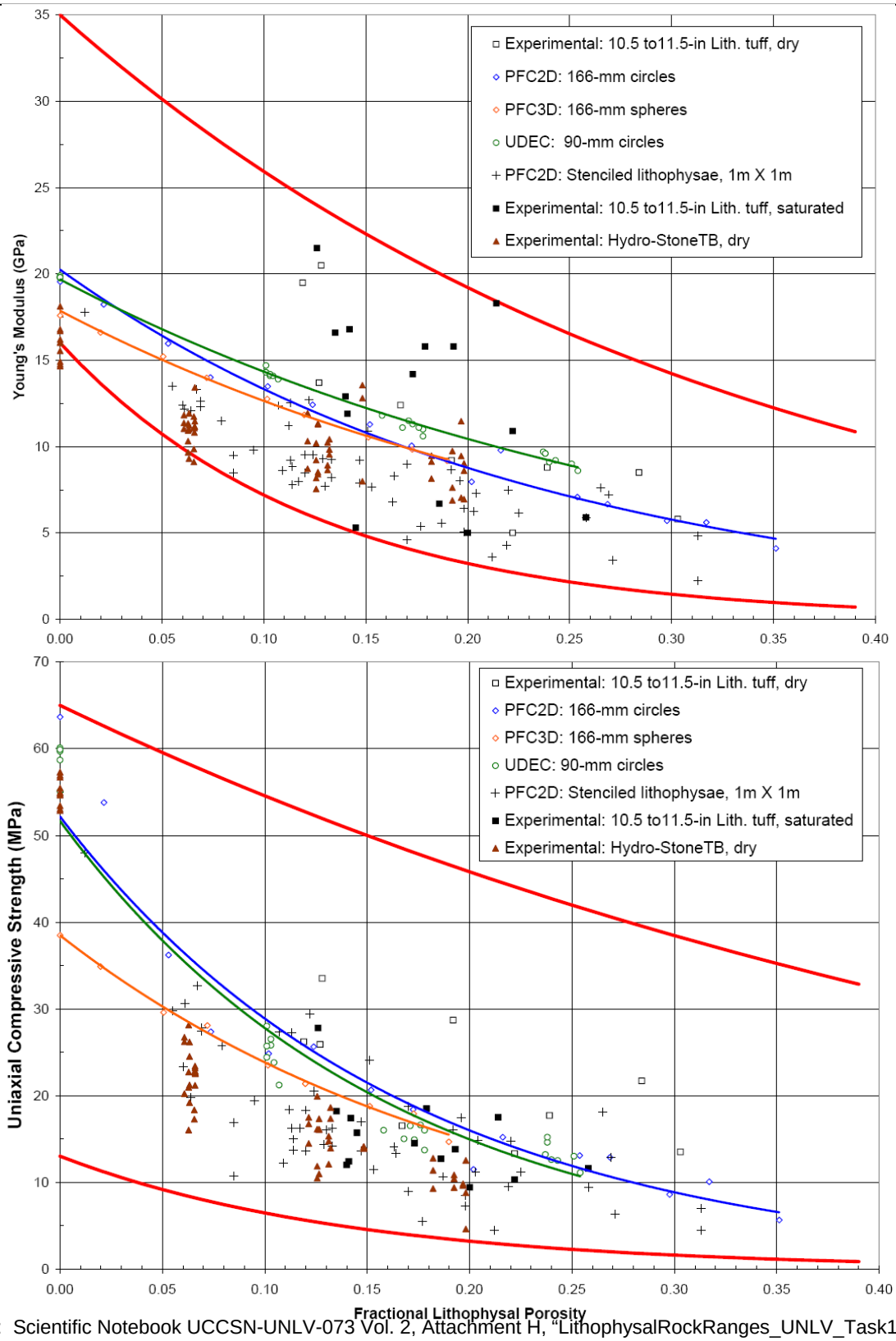

Source: Scientific Notebook UCCSN-UNLV-073 Vol. 2, Attachment H, "LithophysalRockRanges_UNLV_Task13.xls", worksheets "E-por (UNLV)" and "q-por (UNLV)". For comparative purposes only, not to be used for quality-affecting work.

Figure 7-16. PFC & UDEC Numerical Predictions, Tuff and Analog Rock Results with Void Porosity (UQ)

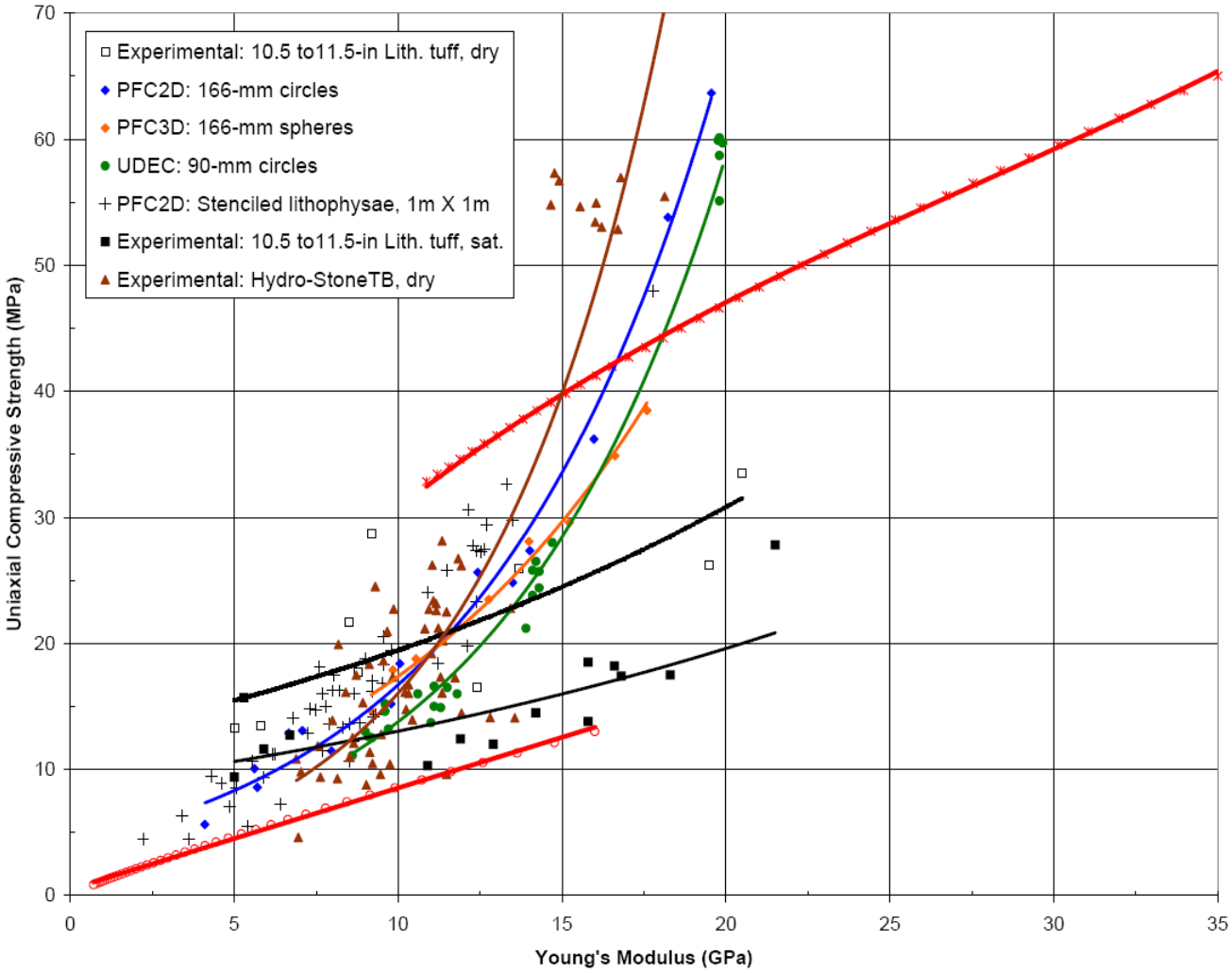

Source: Scientific Notebook UCCSN-UNLV-073 Vol. 2, Attachment H, "LithophysalRockRanges_UNLV_Task13.xls", worksheet "q-E (UNLV)". For comparative purposes only, not to be used for quality-affecting work.

Figure 7-17. PFC & UDEC Numerical Predictions, Tuff and Analog Rock Results, UCS vs. E (UQ)

Rock mass strength categories for lithophysal rock were developed by YM project personnel and were related to percent lithophysal porosity (Rigby, D.B. 2004, Table 6.4-1 and Figure 6.4-5). The weakest rock mass category was category 1 and represented more than 25 percent lithophysal porosity. Categories 2 through 5 corresponded to 20-25 percent, 15-20 percent, 10-15 percent and less than 10 percent lithophysal porosity, respectively. Hydro-Stone TB® specimen porosity groups (19, 13, and 7 percent) targeted rock mass categories 3, 4, and 5, which represented more than 75 percent of the rock found along the ECRB Cross-Drift (Rigby, D.B. 2004, Figure 6.4-8).

Assuming that the experimental Hydro-Stone TB® behavior is sufficiently close to that of actual lithophysal tuff, the Hydro-Stone TB® results (holes only) can be superposed on a plot of the rock mass categories (Rigby, D.B. 2004, Figure 6.6-5) and this is done on Figure 7-18. It can be seen that the Hydro-Stone TB® results plot between the project's upper and lower bounds, generally plot above the 10 MPa strength cutoff value, and correspond to lithophysal rock mass categories 2

through 4, and follows the trend of the "panel map" specimen numerical predictions (crosses in Figure 7-18). So, the Hydro-Stone TB® specimens give mechanical strength results that are about one rock mass category lower than is expected based on their lithophysal porosity.

It is likely that if Hydro-Stone TB® specimens were created with greater than 20 percent hole porosity, then they may plot below the 10 MPa strength cutoff value. However, solid Hydro-Stone TB® specimens do have a slightly lower strength than that estimated for nonlithophysal rock and three-dimensional porosity specimens would have higher strength than the two-dimensional specimens (holes running all the way through) used in this research.

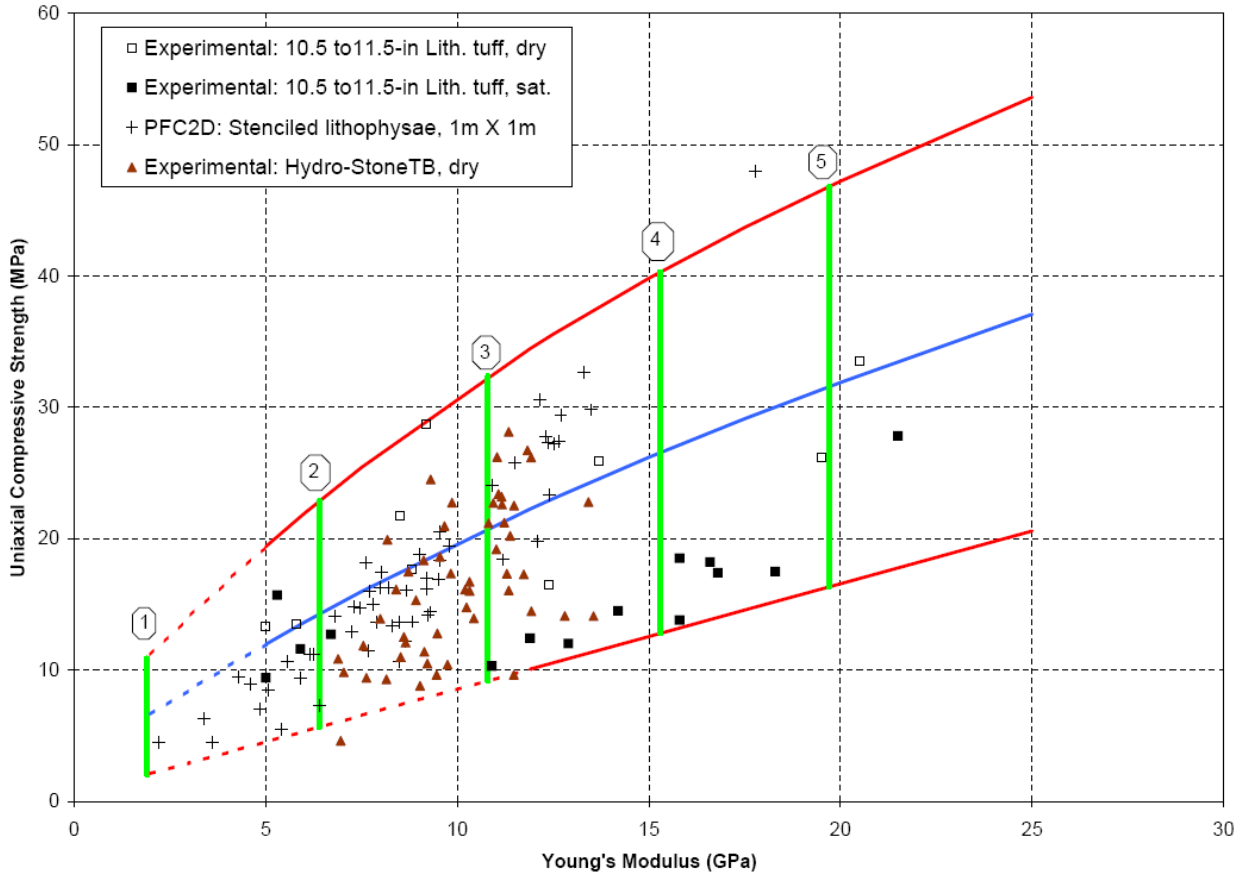

Source: Scientific Notebook UCCSN-UNLV-073 Vol. 2, Attachment H, "LithophysalRockRanges_UNLV_Task13.xls", worksheet "Bounds (cat, UNLV)". For comparative purposes only, not to be used for quality-affecting work.

Figure 7-18. Lithophysal Rock Mass Categories and Test Results, UCS vs. E (UQ)

Summary. The manner and nature of failure observed during experimental testing was consistent with that predicted by the numerical models. The analog rock experimental data does not confirm the numerical prediction of Young's modulus being dependent on void shape, however, the experimental data confirms that void shape does influence uniaxial strength. For all values of void porosity, experimental scatter in mechanical properties is significantly greater than that predicted by the numerical models. The normalized experimental data provides a reasonable match to numerical predictions for the modulus versus void porosity plot, but is not a good match for the strength versus void porosity plot, since experimental data is essentially a lower bound to the numerical predictions. The experimental data also plot below the numerical predictions in the normalized strength versus modulus plot. A bilinear model appears to fit the analog rock experimental data better than an exponential curve. When the Hydro-StoneTB® experimental results are plotted on Yucca Mountain project bounding plots, the experimental data overlap numerical predictions of "panel map" specimens. Hydro-Stone TB® specimens give mechanical strength results that are about one rock mass category lower than is expected based on their lithophysal porosity.

7.2 Conclusions Based Only on Q Data

Uniaxial testing of ten solid specimens of Hydro-Stone TB® yielded sudden and catastrophic brittle failure averaging a Young's modulus of 16 GPa, Poisson's ratio of 0.28, and an average ultimate strength of 55 MPa. This stiffness and strength is close to but slightly lower than the same property values of actual tuff.

The Hydro-Stone TB® uniaxial experimental results show that as void porosity increases, both the Young's modulus and ultimate strength values decrease. The void porosity is the primary physical property useful for predicting mechanical properties, more significant than size of hole or shape of hole. At similar void porosities, there is higher scatter in strength results than for Young's modulus values. The modulus and strength with void porosity relationships are essentially linear over the 5 to 20 percent void porosity range. When zero void porosity (solid specimen) results are added, exponential functions do not provide a good fit to the data. The percent change in modulus from the solid specimen value is roughly 30 and 45 percent at 7 and 19 percent void porosity, respectively. From solid specimens there is roughly a 60 percent drop in strength with about 7 percent void porosity, increasing to an 80 percent drop at about 20 percent void porosity. A linear relationship exists between modulus and strength, although a fair amount of scatter is seen. Patterns A, B, and C in this research each give basically the same statistical trends and results.

No dependence of Young's modulus on void hole size is discernable. There may be a slight dependence of uniaxial strength on void hole size; smaller hole specimens tend to have higher strengths.

The experimental data showed no dependence of Young's modulus on void hole shape, but a moderate correlation between strength and void shape. It is likely that the shape dependence is related to both orientation of the shapes and average bridge length.

An exponential curve is not a good fit to the normalized experimental data (modulus and strength with void porosity). A bilinear model gives a much better fit to the normalized data.

Young's modulus determinations resulted in tangent at 50% having the highest value, best fit over 25 to 50% giving an intermediate value, and the 0 to 50% secant value giving the lowest Young's modulus. It is recommended that the best fit Young's modulus (25 to 50%) be used.

7.3 Corroboration Based on Q Scientific Notebook Data

The observed uniaxial stress-strain behavior of Hydro-Stone TB® specimens with holes was linear elastic up to a stress of about 75 percent of ultimate strength. Specimen failure is achieved by a series of local failures with progressive cracking between holes and edges of the specimen, but generally, most (and sometimes all) visible cracking occurs at the time of ultimate loading. The final failure pattern was typically a combination of tensile splitting and diagonal shear. A plane strain condition of specimens was noted with similar cracking patterns visible on both the front and back sides of specimens.

The replicate specimen tests generally yielded similar patterns of failure (both in location and number of progressive cracks and final cracking patterns). Replicate tests also had relatively similar values of strength and modulus.

7.4 Corroboration Based on UQ Data

The manner and nature of failure observed during experimental testing was consistent with that predicted by the numerical models. The analog rock experimental data does not confirm the numerical prediction of Young's modulus being dependent on void shape, however, the experimental data confirms that void shape does influence uniaxial strength. For all values of void porosity, experimental scatter in mechanical properties is significantly greater than that predicted by the numerical models. The normalized experimental data provides a reasonable match to numerical predictions for the modulus versus void porosity plot, but is not a good match for the strength versus void porosity plot since experimental data is essentially a lower bound to the numerical predictions. The experimental data also plots below the numerical predictions in the normalized strength versus modulus plot. A bilinear model appears to fit the analog rock experimental data better than an exponential curve. When the Hydro-StoneTB® experimental results are plotted on Yucca Mountain project bounding plots, the experimental data overlaps numerical predictions of "panel map" specimens. Hydro-Stone TB® specimens give mechanical strength results that are about one rock mass category lower than is expected based on their lithophysal porosity.

8.0 INPUTS AND REFERENCES

8.1 Inputs

Figure	Data ID Number (DID)	Worksheet Name
7-7	013DR.002	Plots
7-8	013DR.002	Plots
7-10	013DR.002	Plots
7-11	013DR.002	Plots
7-12	013DR.002	Plots
Table		
7-1	013DR.002	QA Data Summary
7-2	013DR.002	QA Data Summary
7-3	013DR.002	All data
7-4	013DR.002	Data by porosity
7-5	013DR.002	Data by porosity
7-6	013DR.002	Data by porosity

Yucca Mountain Laboratory Mechanical Test Data

A primary source document that compiles the mechanical testing data (Young's modulus and compressive strength are used in this report) on Topopah Spring Tuff is the *Subsurface Geotechnical Parameters Report* (Rigby, D.B.,et. al. 2003). The specific data sources used that have porosity measurements associated with the tested rock specimens are listed in Table 8-1. These data are used as direct inputs in Sections 4.2 and 7.1.9 of this report (the data is plotted in Figures for comparison purposes only). The results from large diameter lithophysal samples better reflect the behavior of the in situ rock since they can include more representative lithophysae than smaller samples. This calculation also includes a description of numerical studies and the original data supporting this numerical analysis.

Lithophysal Rock Mass Mechanical Properties of the Repository Host Horizon (Rigby, D.B. 2004) is a calculation using the above primary source DTN data for inputs to analysis and for making plots. This includes both the experimental results from uniaxial tests on large core lithophysal tuff and numerical results of numerical uniaxial tests on numerical models of lithophysal tuff. As indicated in this report, figures from BSC 2004 have been adopted and the format modified to match the format of this report.

Table 8-1. DTNs of Tested Rock Specimens Having Porosity Data

Yucca Mountain Mechanical Tests on Rock Specimens with Porosity Data		
Source of Rock	**Size Specimen (Diameter)**	**DTNs**
Busted Butte cores	267 mm (10.5-in)	SNSAND84086000.000
ESF and ECRB Cross-Drift	290 mm (11.5-in)	SN0208L0207502.001, SN0211L0207502.002, SN0305L0207502.005, and SN0305L0207502.006

Source: Rigby, D.B., et. al. 2003, Section 8.4. In addition to the above DTNs the DTN of qualified compressive strength values is MO0311RCKPRPCS.003 and DTN of qualified Young's Modulus values is MO0402DQRIRPPR.003.

SN0208L0207502.001. Mechanical Properties of Lithophysal Tuff, Batch #1 (Test Dates: July 31, 2002 through August 16, 2002). Submittal date: 08/20/2002.

SN0211L0207502.002. Mechanical Properties of Lithophysal Tuff, Batch #2 (Test Dates: October 22, 2002 through October 25, 2002). Submittal date: 11/13/2002.

SN0305L0207502.005. Material Abundances from Point Counts on Laboratory Mechanical Property Specimens for Batch #1 and Batch #2. Submittal date: 05/20/2003.

SN0305L0207502.006. Porosity of Laboratory Mechanical Properties Test Specimens for Batch #1 and Batch #2. Submittal date: 05/20/2003.

PFC and UDEC Numerical Modeling of Lithophysal Rock

Numerical modeling of the mechanical behavior of lithophysal rock from the Topopah Spring Tuff is discussed in Rigby, D.B., et. al. 2003 (Sections 9.1, 9.2, and Attachments V, VI, and VIII) and Rigby, D.B. 2004 (Section 6.5). For the simulations that used the software code PFC2D, these data are taken from the files *shapestudy.xls* and *shapestudy_bf2-bf4.xls* (Rigby, D.B., et. al. 2003, Attachment VIII, CD#2 "PFC_runs\ShapeStudy\shapestudy.xls" and "PFC_runs\ShapeStudy\shapestudy_bf2-bf4.xls"). For the simulations that used the software code UDEC, these data are taken from the file *Summary2_newest.xls* (Rigby, D.B., et. al. 2003, Attachment VIII, CD#20 "UDEC_CD1\Summary2_newest.xls").

8.2 Cited References

ASTM D 4543 (2001). *Standard Practices for Preparing Rock Core Specimens and Determining Dimensional and Shape Tolerances.* West Conshohocken, Pennsylvania: American Society for Testing and Materials.

Avar, B.B. (2003). *The Influence of Lithophysal Porosity on the In-Situ Stress-Strain Properties of Topopah Spring Tuff.* NSHE Technical Report No. TR-02-008. Las Vegas, Nevada: UNLV.

Avar, B.B., N. Hudyma, and M. Karakouzian (2003). *Porosity Dependence of the Elastic Modulus of Lithophysae-rich Tuff: Numerical and Experimental Investigations.* Int. J. of Rock Mech. & Mining Sciences 40 (2003), pp. 919-928.

Brown, E.T., ed. (1981). *Rock Characterization Testing & Monitoring, ISRM Suggested Methods.* New York, New York: Pergamon Press.

Elwell, D.J. and G. Fu (1995). *Compression Testing of Concrete: Cylinders vs. Cubes*. Special Report 119, Engineering Research and Development Bureau, New York State Dept. of Transportation, March 1995. Conducted in cooperation with the U.S. Dept. of Transportation, Federal highway Administration.

Hoek, E. and E.T. Brown (1980). *Underground Excavations in Rock.* Institution of Mining and Metallurgy. London.

Hudyma, N., B.B. Avar, and M. Karakouzian (2004). *Compressive Strength and Failure Modes of Lithophysae-rich Topopah Spring Tuff Specimens and Analog Models Containing Cavities.* Engineering Geology 73 (2004), pp. 179-190.

Kicker, D. (2004). *Drift Degradation Analysis.* ANL-EBS-MD-000027 Rev. 03. Las Vegas, Nevada: Bechtel SAIC Company. ACC: DOC.20040915.0010. http://www.osti.gov/energycitations/product.biblio.jsp?query_id=5&page=0&osti_id=837516

Price, R.H. (1983). *Analysis of the Rock Mechanics Properties of Volcanic Tuff Units from Yucca Mountain, Nevada Test Site.* SAND82-1315. Albuquerque, New Mexico: Sandia National Laboratories. ACC: NNA.19870406.0181.

Price, R.H. (1986). *Effects of Sample Size on the Mechanical Behavior of Topopah Spring Tuff.* SAND85-0709. Albuquerque, New Mexico: Sandia National Laboratories. ACC: NNA.19891106.0125.

Price, R.H. (2004). *The Mechanical Properties of Lithophysal Tuff: Laboratory Experiments.* TDR-EBS-MD-000027 REV 00. Las Vegas, Nevada: Bechtel SAIC Company. ACC: DOC.20040506.0001.

Read, H.E. and G.A. Hegemier (1984). *Strain Softening of Rock, Soil and Concrete – A Review Article.* Mechanics of Materials, Vol. 3, pp. 271-294. Elsevier Science publishers B.V.

Rigby, D.B., et. al. (2003). *Subsurface Geotechnical Parameters Report.* 800-K0C-WIS0-00400-000-00A. Las Vegas, Nevada: Bechtel SAIC Company. ACC: ENG.20040108.0001. http://www.osti.gov/energycitations/product.biblio.jsp?query_id=5&page=0&osti_id=837518

Rigby, D.B. (2004). *Lithophysal Rock Mass Mechanical Properties of the Repository Host Horizon.* 800-K0C-SS00-00200-000-00A. Las Vegas, Nevada: Bechtel SAIC Company. ACC:

ENG.20041111.0001.
http://www.osti.gov/energycitations/product.biblio.jsp?query_id=5&page=0&osti_id=837709

USG Gypsums (no date listed). *USG Gypsums*. Retrieved April 11, 2007 from www.sculpturesupply.com/sscpdfs/gypsums.pdf.

9.0 SOFTWARE

9.1 How Nonexempt Software was Used to Produce Data (QAP-3.2)

No nonexempt software was used to produce any data as part of this research. This section is "not applicable".

9.2 How Exempt Software was Used to Produce Data

Microsoft Excel 2003 SP2 was used to reduce data, summarize the data, determine statistics for the data, and plot the data.

10.0 APPENDICES

A list of Appendices is provided in Table 10-1, including the number, title, and total pages for each Appendix.

Table 10-1. List of Appendices

Appendix Letter	Appendix Title	Number of Pages
A	Specimen Description and Naming Convention	8
B	Replication Examples Showing Final Cracking Patterns and Properties (UQ)	3

APPENDIX A

SPECIMEN DESCRIPTION AND NAMING CONVENTION

SPECIMEN DESCRIPTION AND NAMING CONVENTION

Figure A-1 shows examples of specific planned specimen patterns from the tables that follow (Tables A-1 to A-8). Further details are available in scientific notebook UCCSN-UNLV-073 Vol. 2.

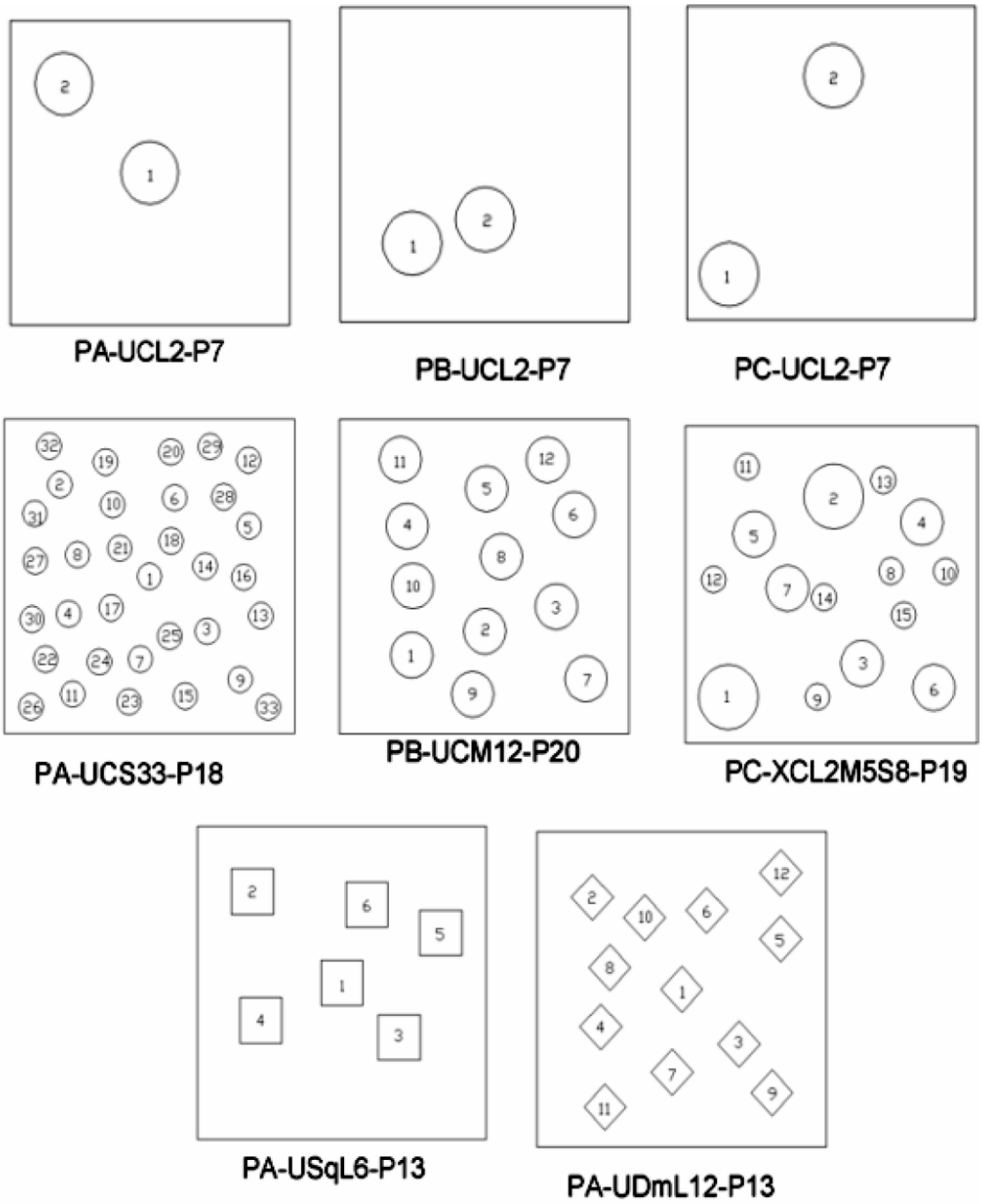

Figure A-1. Examples of Specimen Hole Patterns including their Sample I.D. Names

Figure A-2 shows photos of actual Hydro-StoneTB® specimens that were created based on the planned patterns shown in Figure A-1.

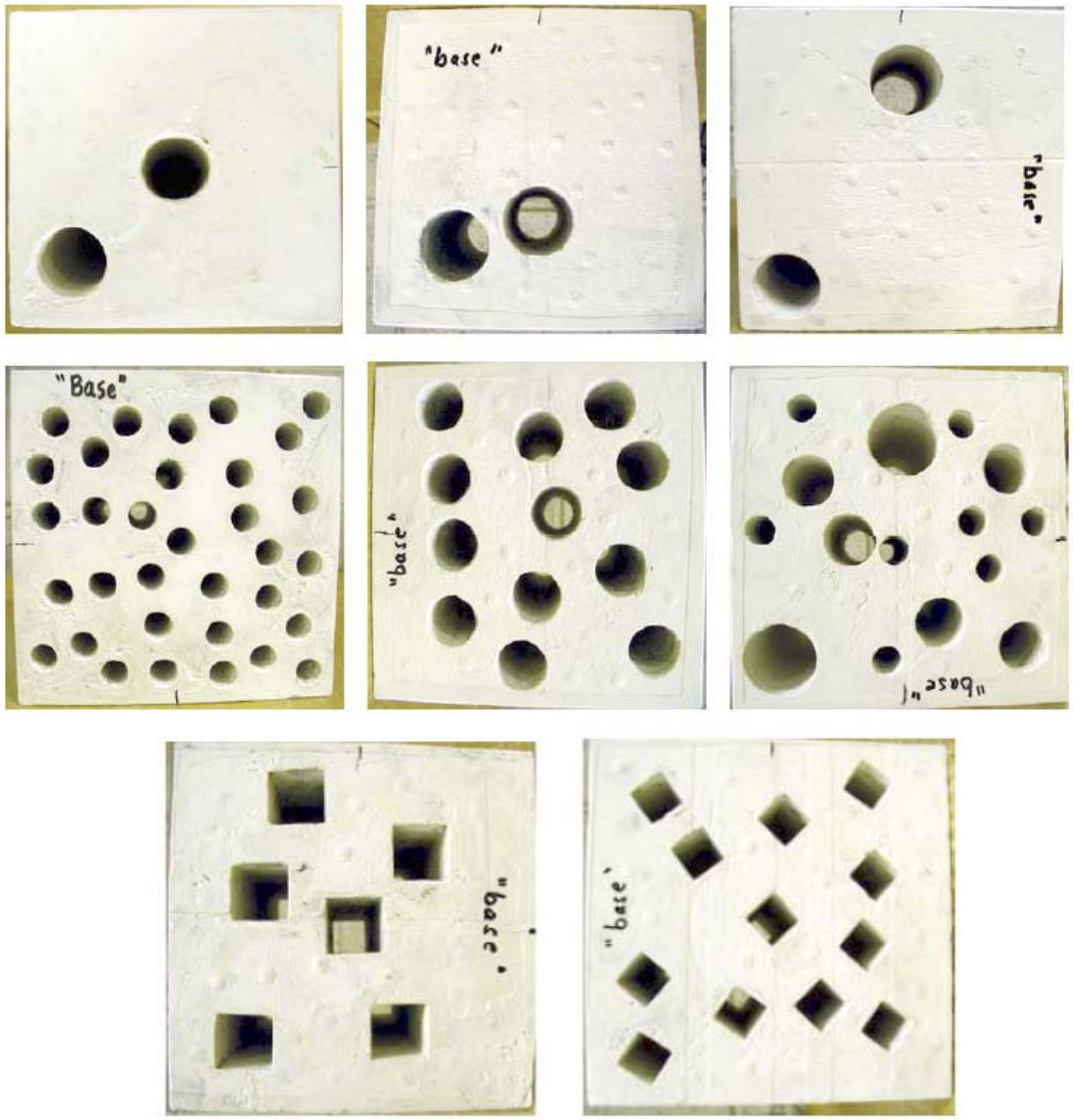

Note: some specimen photos above may need to be rotated to match the corresponding pattern in Fig. A-1.

Figure A-2. Photos of Actual Specimens Produced following Figure A-1 Patterns

Table A-1: Specimens Containing Circular Holes (Pattern A)

Hole Shape	Starting Hole Location	Hole Size			Number of Holes	Porosity (%)	Specimen's Name
Circle	at center (0,0)	Uniform		1.226" (L)	2	6.56	QA-PA-UCL2-P7
					4	13.12	QA-PA-UCL4-P13
					6	19.68	QA-PA-UCL6-P20
				0.870" (M)	4	6.61	QA-PA-UCM4-P7
					8	13.21	QA-PA-UCM8-P13
					12	19.82	QA-PA-UCM12-P20
				0.503" (S)	11	6.07	QA-PA-UCS11-P6
					22	12.14	QA-PA-UCS22-P12
					33	18.22	QA-PA-UCS33-P18
		Mixed	I	L	1	6.59	QA-PA-XCL1M1S3-P7
				M	1		
				S	3		
			II	L	2	14.83	QA-PA-XCL2M3S6-P15
				M	3		
				S	6		
			III	L	2	19.24	QA-PA-XCL2M5S8-P19
				M	5		
				S	8		

Source: Modified from table in scientific notebook UCCSN-UNLV-073 Vol. 2, p. 23. "Porosity (%)" and Specimen's Name come from DID 013DR.002, worksheet "QA Data Summary", columns "DD" and "A", respectively.

The following are the specimen name codes used to build specific specimen names:

- **QA** = prepared with QA Procedures, **NQ** = not following QA Procedures
- **PA** = Pattern A, **PB** = Pattern B, or **PC** = Pattern C (see Figure A-1)
- **U** = Uniform (all holes same size) or **X** = Mixed (different size holes)
- Shape of hole: **C** = Circular, **Sq** = Square, **Dm** = Diamond
- **L** = Large, **M** = Medium, **S** = Small (size of hole, followed by number of holes)
- **P** = approximate void porosity of specimen (%)
- A letter is appended to the end of each specimen name to differentiate between specimens of the exact same pattern: **A** for the first specimen, **B** for the second specimen, **C** for the third, and so on.

Table A-2: Specimens Containing Circular Holes (Pattern B)

Hole Shape	Starting Hole Location	Hole Size			Number of Holes	Porosity (%)	Specimen's Name
Circle	(-1.5, -1.5)	Uniform		1.226" (L)	2	6.56	QA-PB-UCL2-P7
					4	13.12	QA-PB-UCL4-P13
					6	19.68	QA-PB-UCL6-P20
				0.870" (M)	4	6.61	QA-PB-UCM4-P7
					8	13.21	QA-PB-UCM8-P13
					12	19.82	QA-PB-UCM12-P20
				0.503" (S)	11	6.07	QA-PB-UCS11-P6
					22	12.14	QA-PB-UCS22-P12
					33	18.22	QA-PB-UCS33-P18
		Mixed	I	L	1	6.59	QA-PB-XCL1M1S3-P7
				M	1		
				S	3		
			II	L	2	14.83	QA-PB-XCL2M3S6-P15
				M	3		
				S	6		
			III	L	2	19.24	QA-PB-XCL2M5S8-P19
				M	5		
				S	8		

Source: Modified from table in scientific notebook UCCSN-UNLV-073 Vol. 2, p. 24. "Porosity (%)" and Specimen's Name come from DID 013DR.002, worksheet "QA Data Summary", columns "DD" and "A", respectively.

Note: The starting hole location coordinates (x, y) are measured in inches from the center of the specimen.
See Table A-1 for specimen name code definitions.

Table A-3: Specimens Containing Circular Holes (Pattern C)

Hole Shape	Starting Hole Location	Hole Size			Number of Holes	Porosity (%)	Specimen's Name
Circle	(-2.125, -2.125)	Uniform		1.226" (L)	2	6.56	QA-PC-UCL2-P7
					4	13.12	QA-PC-UCL4-P13
					6	19.68	QA-PC-UCL6-P20
				0.870" (M)	4	6.61	QA-PC-UCM4-P7
					8	13.21	QA-PC-UCM8-P13
					12	19.82	QA-PC-UCM12-P20
				0.503" (S)	11	6.07	QA-PC-UCS11-P6
					22	12.14	QA-PC-UCS22-P12
					33	18.22	QA-PC-UCS33-P18
		Mixed	I	L	1	6.59	QA-PC-XCL1M1S3-P7
				M	1		
				S	3		
			II	L	2	14.83	QA-PC-XCL2M3S6-P15
				M	3		
				S	6		
			III	L	2	19.24	QA-PC-XCL2M5S8-P19
				M	5		
				S	8		

Source: Modified from table in scientific notebook UCCSN-UNLV-073 Vol. 2, p. 25. "Porosity (%)" and Specimen's Name come from DID 013DR.002, worksheet "QA Data Summary", columns "DD" and "A", respectively.

Note: The starting hole location coordinates (x, y) are measured in inches from the center of the specimen.
See Table A-1 for specimen name code definitions.

Table A-4: Specimens Containing Square Holes (Pattern A)

Hole Shape	Starting Hole Location	Hole Size		Number of Holes	Porosity (%)	Specimen's Name
Square	at center (0,0)	Uniform	0.868" (L)	3	6.28	QA-PA-USqL3-P7
				6	12.56	QA-PA-USqL6-P13
			0.616" (M)	6	6.32	QA-PA-USqM6-P6
				12	12.65	QA-PA-USqM12-P13

Source: Modified from table in scientific notebook UCCSN-UNLV-073 Vol. 2, p. 26. "Porosity (%)" and Specimen's Name come from DID 013DR.002, worksheet "QA Data Summary", columns "DD" and "A", respectively.

Note: The starting hole location coordinates (x, y) are measured in inches from the center of the specimen.
See Table A-1 for specimen name code definitions.

Table A-5: Specimens Containing Square Holes (Pattern B)

Hole Shape	Starting Hole Location	Hole Size		Number of Holes	Porosity (%)	Specimen's Name
Square	(-1.5, -1.5)	Uniform	0.868" (L)	3	6.28	QA-PB-USqL3-P7
				6	12.56	QA-PB-USqL6-P13
			0.616" (M)	6	6.32	QA-PB-USqM6-P6
				12	12.65	QA-PB-USqM12-P13

Source: Modified from table in scientific notebook UCCSN-UNLV-073 Vol. 2, p. 26. "Porosity (%)" and Specimen's Name come from DID 013DR.002, worksheet "QA Data Summary", columns "DD" and "A", respectively.

Note: The starting hole location coordinates (x, y) are measured in inches from the center of the specimen.
See Table A-1 for specimen name code definitions.

Table A-6: Specimens Containing Diamond Holes (Pattern A)

Hole Shape	Starting Hole Location	Hole Size		Number of Holes	Porosity (%)	Specimen's Name
Diamond	at center (0,0)	Uniform	0.868" (L)	3	6.28	QA-PA-UDmL3-P7
				6	12.56	QA-PA-UDmL6-P13
			0.616" (M)	6	6.32	QA-PA-UDmM6-P6
				12	12.65	QA-PA-UDmM12-P13

Source: Modified from table in scientific notebook UCCSN-UNLV-073 Vol. 2, p. 26. "Porosity (%)" and Specimen's Name come from DID 013DR.002, worksheet "QA Data Summary", columns "DD" and "A", respectively.

Note: The starting hole location coordinates (x, y) are measured in inches from the center of the specimen.
See Table A-1 for specimen name code definitions.

Table A-7: Specimens Containing Diamond Holes (Pattern B)

Hole Shape	Starting Hole Location	Hole Size		Number of Holes	Porosity (%)	Specimen's Name
Diamond	(-1.5, -1.5)	Uniform	0.868" (L)	3	6.28	QA-PB-UDmL3-P7
				6	12.56	QA-PB-UDmL6-P13
			0.616" (M)	6	6.32	QA-PB-UDmM6-P6
				12	12.65	QA-PB-UDmM12-P13

Source: Modified from table in scientific notebook UCCSN-UNLV-073 Vol. 2, p. 26. "Porosity (%)" and Specimen's Name come from DID 013DR.002, worksheet "QA Data Summary", columns "DD" and "A", respectively.

Note: The starting hole location coordinates (x, y) are measured in inches from the center of the specimen.
See Table A-1 for specimen name code definitions.

Table A-8: Solid Specimens (No Holes)

Hole Shape	Starting Hole Location	Hole Size	Number of Holes	Porosity (%)	Specimen's Name
N/A	N/A	N/A	0	0.0	QA-Solid-P0

Source: Modified from table in scientific notebook UCCSN-UNLV-073 Vol. 2, p. 26. "Porosity (%)" and Specimen's Name come from DID 013DR.002, worksheet "QA Data Summary", columns "DD" and "A", respectively.

Note: P0 stands for a void porosity of zero.

APPENDIX B

REPLICATION EXAMPLES SHOWING FINAL CRACKING PATTERNS AND PROPERTIES (UQ)

REPLICATION EXAMPLES SHOWING FINAL CRACKING PATTERNS AND PROPERTIES (UQ)

Figures B-1 and B-2 illustrate further examples of replicate similarity, in addition to the photos provided in Sections 7.1.1 and 7.1.2 of this report. The specimen pattern name is given, followed by the Young's modulus value for each specimen, the average Young's modulus for these specimens, the ultimate strength values for each specimen, and the average strength for this pattern. It can be seen that final cracking patterns and mechanical properties are similar.

QA-PC-UCL2-P7-A, B, C E = 10.1, 9.46, 9.99 Eave = 9.86 GPa UCS = 19.1, 24.2, 24.9 UCSave = 22.7 MPa

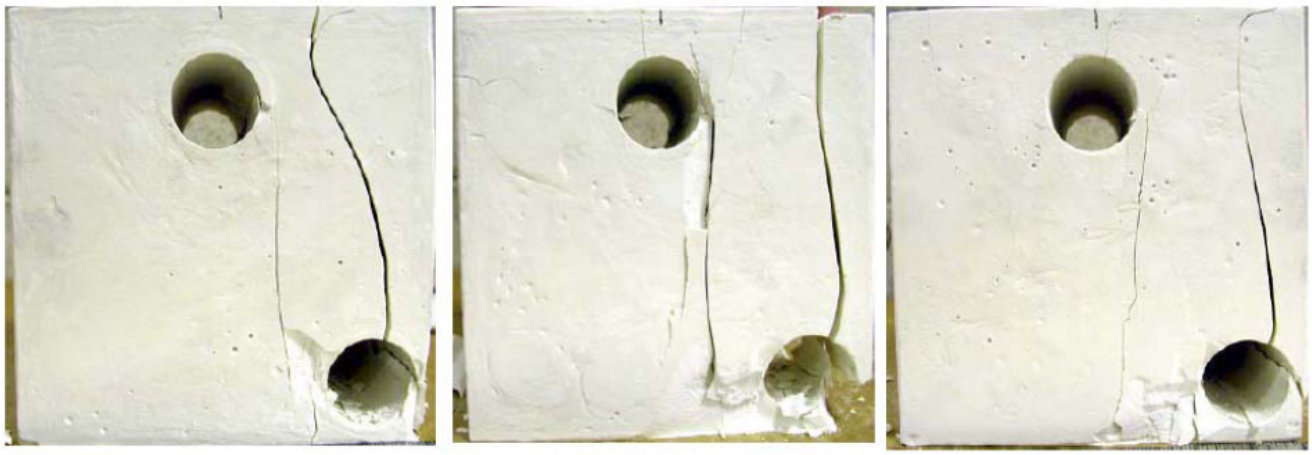

QA-PA-USqM12-P13-A, B, C E = 10.3, 12.8, 10.8 Eave = 11.3 GPa UCS = 16.2, 17.4, 18.4 UCSave = 17.3 MPa

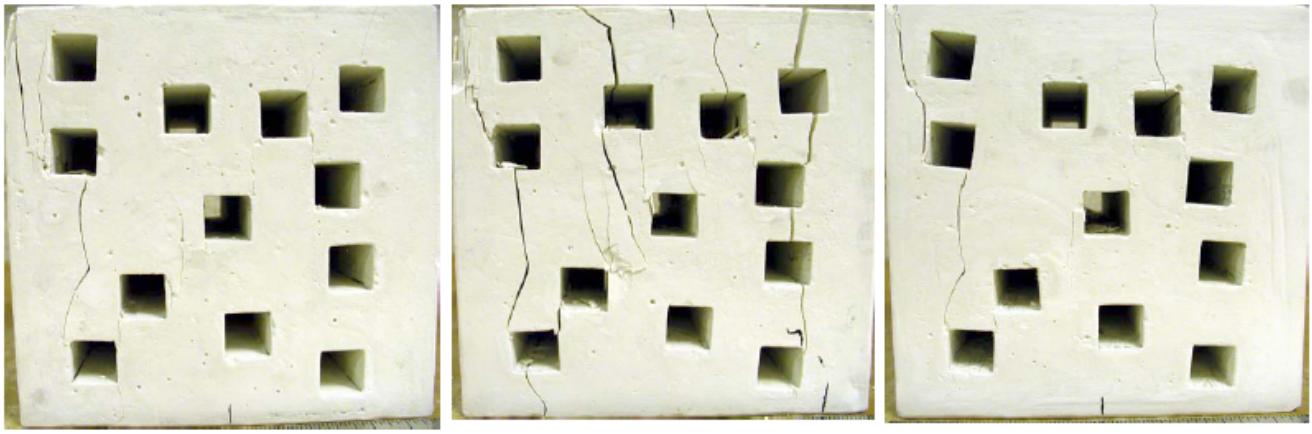

Source: Replicate E and UCS values come from scientific notebook UCCSN-UNLV-073 Vol. 2; worksheet "Data" in file "HydroStone Uniaxial and Porosity Data.xls." Eave and UCSave values come from DID 013DR.002, worksheet "QA Data Summary" or worksheet "QA Data Summary" in file "HydroStone Uniaxial and Porosity Data.xls." For information only, not to be used for quality-affecting work.

Note: E is Young's modulus, Eave is the average E, UCS is the uniaxial compressive strength, UCSave is the average UCS.

Figure B-1. More Examples of Replicate Specimen Behavior (UQ)

QA-PA-UCS11-P6-A, B, C E = 11.9, 11.2, 9.96 Eave = 11.0 GPa UCS = 26.7, 27.9, 24.0 UCSave = 26.2 MPa

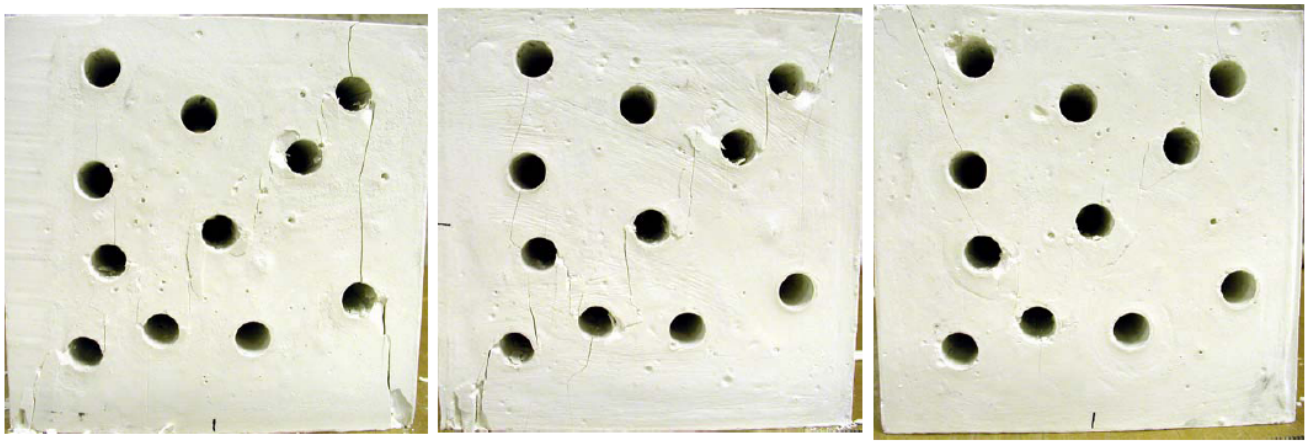

QA-PB-UCS11-P6-A, B, C E = 13.4, 11.4, 10.7 Eave = 11.8 GPa UCS = 25.4, 28.9, 25.9 UCSave = 26.7 MPa

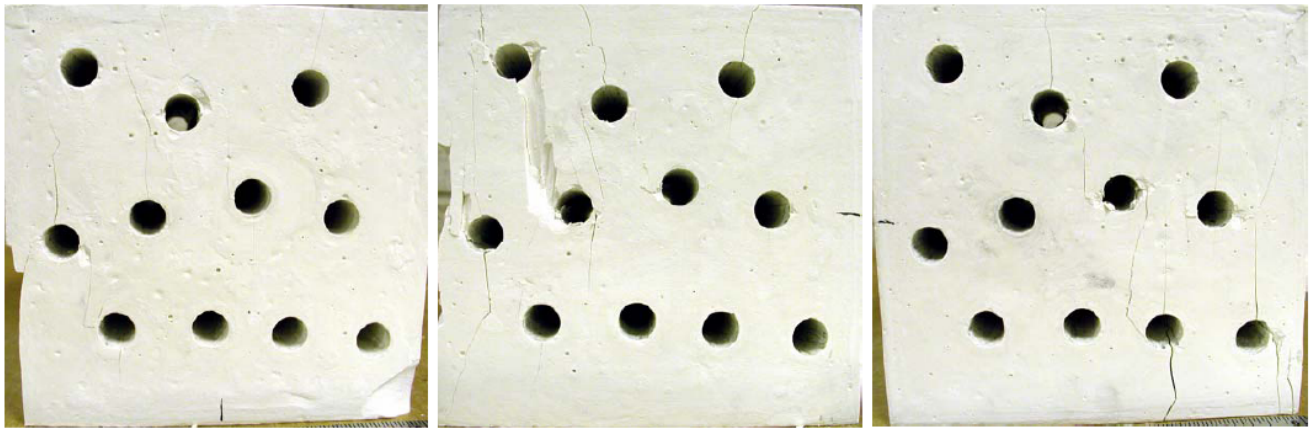

QA-PC-UCS11-P6-A, B, C E = 11.3, 11.7, 11.1 Eave = 11.4 GPa UCS = 20.4, 17.5, 22.7 UCSave = 20.2 MPa

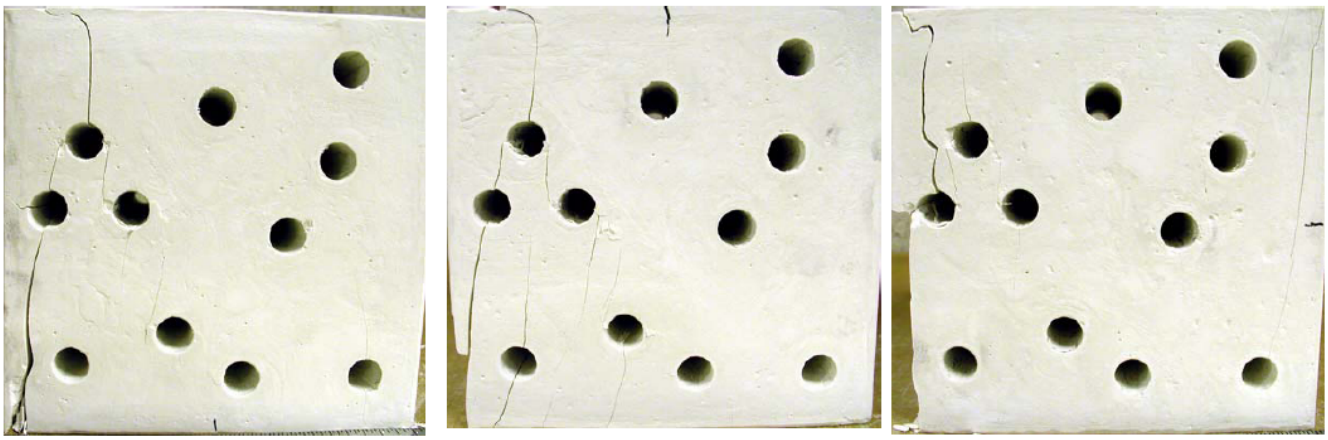

Source: Replicate E and UCS values come from scientific notebook UCCSN-UNLV-073 Vol. 2; worksheet "Data" in file "HydroStone Uniaxial and Porosity Data.xls." Eave and UCSave values come from DID 013DR.002, worksheet "QA Data Summary" or worksheet "QA Data Summary" in file "HydroStone Uniaxial and Porosity Data.xls." For information only, not to be used for quality-affecting work.

Note: E is Young's modulus, Eave is the average E, UCS is the uniaxial compressive strength, UCSave is the average UCS.

Figure B-2. Comparison of UCS11-P6 for Patterns A, B, and C (UQ)